

UTTAC-77, 2008

UTTAC

ANNUAL REPORT 2007

TANDEM ACCELERATOR COMPLEX
Research Facility Center for Science and Technology
University of Tsukuba

<http://www.tac.tsukuba.ac.jp/>

UTTAC

ANNUAL REPORT 2007

April 1, 2007 – March 31, 2008

UTTAC-77 2008

Executive Editor: Hiroshi Kudo

Editors: Yoshihiro Yamato, Daiichiro Sekiba, Kimikazu Sasa, Tetsuro Komatsubara

UTTAC is a series of issues, which include annual reports of Tandem Accelerator Complex, Research Facility Center for Science and Technology, University of Tsukuba.

The issues may also include irregular reports written by English.

Copyright © 2008 by Tandem Accelerator Complex, Research Facility Center for Science and Technology, University of Tsukuba and individual contributors.

All reports are written on authors' responsibility and thus the editors are not liable for the contents of the report.

Tandem Accelerator Complex, Research Facility Center for Science and Technology,
University of Tsukuba

Tennodai 1-1-1, Tsukuba, Ibaraki 305-8577, Japan

<http://www.tac.tsukuba.ac.jp/>
annual@tac.tsukuba.ac.jp

PREFACE

This annual report covers researches carried out at University of Tsukuba Tandem Accelerator Complex (UTTAC) during the fiscal year 2007 (1 April 2007 ~ 31 March 2008). The topics include not only accelerator-based researches using the 12MV Pelletron and 1MV Tandatron accelerators, but also closely related researches to UTTAC.

July 15, 2008

Editors

CONTENTS

1. ACCELERATOR AND EXPERIMENTAL FACILITIES	
1.1 Accelerator operation 2007	1
1.2 Status of the Tsukuba AMS system	4
1.3 Developments of ERCS hydrogen analysis	6
2. NUCLEAR PHYSICS	
2.1 Production of radioactive nuclear beam of ^8Li and its in-flight identification	9
2.2 $^{118}\text{Sn}(d,p)$ reaction in search for Coulomb stripping of deuteron V	11
2.3 Measurement of the time response in Hybrid Photo Detector II	13
2.4 Study of nuclear synthesis of ^{26}Al by gamma ray spectroscopy	15
2.5 Nuclear structure of supernova neutrino-process isotope ^{138}La	17
3. MATERIALS AND CLUSTER SCIENCE	
3.1 Synthesis of elongated and oriented gold nanorods in silica by irradiation of swift heavy ion	19
3.2 Characterization of Er-doped GaN by heavy ion RBS	21
3.3 Dependence of the vicinage effect on interatomic spacing of carbon clusters	23
3.4 Point defects in Er-doped GaN probed by means of positron annihilation	24
3.5 Rutherford backscattering spectroscopy on Pt-absorbed HOPG surface	26
3.6 Möessbauer study of sub-micron sized Fe_3O_4 particles and NH_3 nitrized particles	28
3.7 Molecular dynamics calculation of water clusters	30
3.8 Simulation of gas aggregation cell by DSMC method	32
4. ACCELERATOR MASS SPECTROMETRY	
4.1 Cosmogenic ^{36}Cl measurements in the Dome Fuji ice core, Antarctica	33
4.2 Residence times of spring waters on the foot of Mt. Fuji, estimated from bomb-produced ^{36}Cl	35
4.3 Measurement of in situ-produced cosmogenic ^{36}Cl in calcite	38
4.4 Depth profile of $^{36}\text{Cl}/^{35}\text{Cl}$ induced in the thick concrete shield in EP-1 beam line at the 12-GeV proton synchrotron facility, KEK	40
4.5 Chlorine-36 in Gibeon iron meteorite	42
5. INTERDISCIPLINARY RESEARCH	
5.1 Development of radiation environment monitor on board spacecraft	43
5.2 Micro-PIXE analysis of rare-earth elements in monazite	45
5.3 Ion induced nanoparticle formation in $\text{N}_2/\text{H}_2\text{O}/\text{SO}_2$	48
6. LIST OF PUBLICATIONS	
6.1 Journals	49
6.2 International conferences	52

7. THESES	53
8. SEMINARS	54
9. SYMPOSIA	55
10. LIST OF PERSONEL	57

1.

ACCELERATOR AND EXPERIMENTAL FACILITIES

1.1 Accelerator operation 2007

K. Sasa, S. Ishii, H. Kimura, H. Oshima, Y. Tajima, T. Takahashi, Y. Yamato, T. Komatsubara, D. Sekiba and H. Kudo.

The University of Tsukuba Tandem Accelerator Complex (UTTAC) operates the 12UD Pelletron tandem accelerator and the 1 MV Tandetron accelerator. The total service time of the UTTAC multi-tandem accelerator facility was 145 days (3,480 hours) in the fiscal year 2007. In this year we have started on the new project “Open Advanced Facilities Initiative for Innovation (Strategic Use by Industry)”, which is supported financially by the Ministry of Education, Culture, Sports, Science and Technology. In this project, 5 industrial research programs were progressed using 18 % (624 hours) of the total service time by industrial users.

The 12UD Pelletron tandem accelerator

During the total service time, the accelerator operating time and the experimental beam time were 1748.3 and 1312.5 hours, respectively. The operating time was about 93.2 % relative to that in 2006. Figure 1 shows the accelerator operation hours per month. The beam time histogram with respect to the terminal voltage is shown in Fig.2. Figure 3 represents the percentage of the operation hours for the three ion sources and ion species.

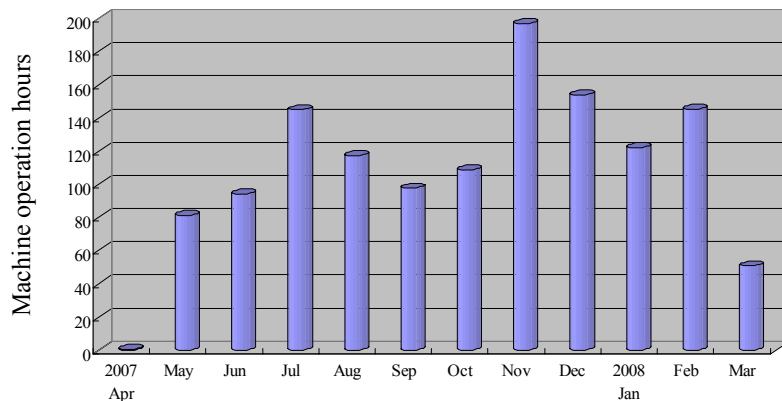


Fig.1. Accelerator operation hours per month for the fiscal year 2007.

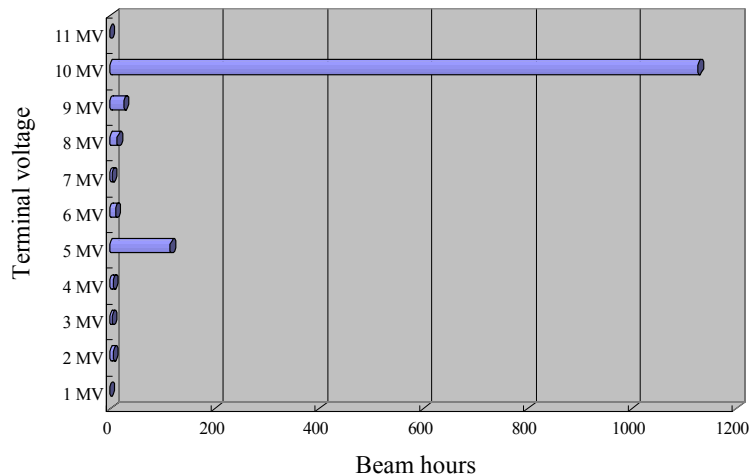


Fig.2. Beam time histogram as a function of the terminal voltage in the fiscal year 2007.

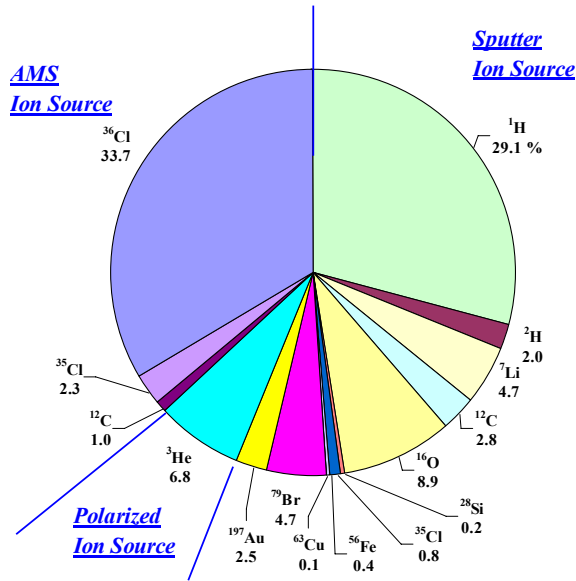


Fig.3. Percentage of the operation hours for the three ion sources and ion species for the fiscal year 2007.

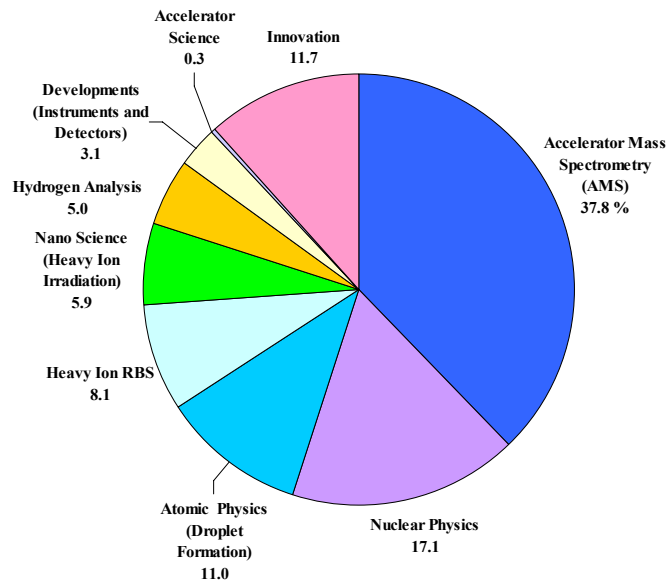


Fig.4. Percentage of the experimental beam time for the running research fields for the fiscal year 2007.

In the year of 2007, 73 research programs were performed and a total of 648 researchers used the 12UD Pelletron tandem accelerator. Fig.4 shows the percentage of the experimental beam time for the running research fields with the 12UD Pelletron tandem accelerator. The AMS study has been the research field of the largest beam time ratio since 2006.

A cooling system of the SF₆ gas compressor was broken and repaired in 2007. We could not transfer SF₆ gas between the accelerator main tank and the storage tank until January 2008. The scheduled maintenance in the spring 2008 was started on March 13. We have a plan to exchange the corona needle to the divided resistor at the next scheduled maintenance. At this maintenance time, we performed an efficiency test on the divided resistor with the terminal voltage of 3 MV by using 3 accelerator column units. The results of the efficiency test demonstrated that the divided resistor had a good performance.

The 1MV Tandetron accelerator

During the total service time, the accelerator operating time and the experimental beam time were 433.1 and 230.0 hours, respectively. The operating time was about 66.4 % relative to that in 2006. In the year of 2007, 38 research programs were performed and a total of 144 researchers used the 1 MV Tandetron accelerator. Figure 5 shows the percentage of accelerated ions with the 1MV Tandetron accelerator. Figure 6 shows the percentage of the experimental beam time for the running research fields. The main research field of the 1MV Tandetron accelerator was cluster beam studies, in which a carbon cluster beam ($C_{n<8}$) was mainly used. The 1MV Tandetron accelerator was also used for trace-element analysis with Particle Induced X-ray Emission (PIXE), Rutherford Backscattering Spectroscopy (RBS), Elastic Recoil Detection Analysis (ERDA) and ion implantation.

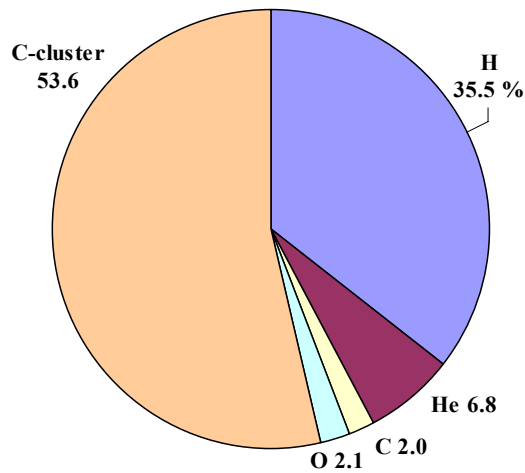


Fig.5. Percentage of accelerated ions with the 1MV Tandetron accelerator for the fiscal year 2007.

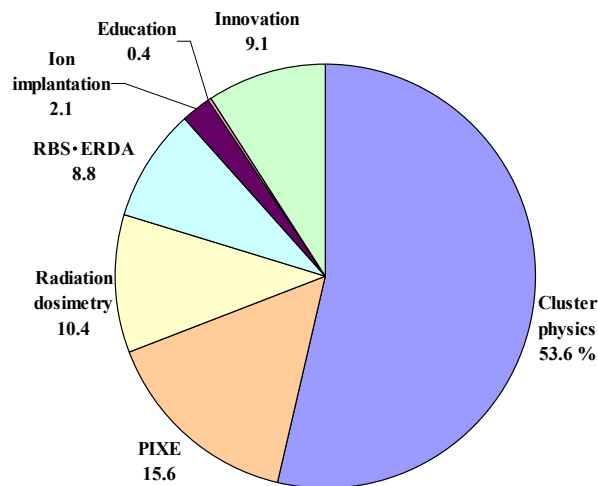


Fig.6. Percentage of the experimental beam time for the running research fields with the 1MV Tandetron accelerator for the fiscal year 2007.

1.2 Status of the Tsukuba AMS system

K. Sasa, Y. Nagashima, T. Takahashi, K. Sueki, Y. Tosaki, M. Tamari, T. Oki, S. Mihara, Y. Guan, Y. Yamato, M. Matsumura, K. Bessho¹, H. Matsumura¹, T. Miura¹, K. Masumoto¹ and Y. Matsushi²

The Tsukuba AMS system has been able to measure environmental levels of long lived radioisotopes of ¹⁴C, ²⁶Al, ³⁶Cl and ¹²⁹I by employing a molecular pilot beam method^[1]. In addition, we have been developing ³²Si and ⁴¹Ca AMS systems for future research programs. In the year of 2007, we measured about 500 samples with the Tsukuba AMS system. Table 1 shows research programs and the number of samples performed by the Tsukuba AMS system.

Table 1 Research programs and the number of samples by the Tsukuba AMS system in the year of 2007.

AMS research programs	Target material	Organization	Number
³⁶ Cl-AMS			
³⁶ Cl in the Dome Fuji ice core, Antarctica	Antarctic ice core	Univ. of Tsukuba	181
³⁶ Cl in the radiation shield at accelerator facilities	Concrete	KEK	48
Bomb-produced ³⁶ Cl as a tracer in groundwater	Hydrological samples (ground water, rain water)	Univ. of Tsukuba	43
In-situ ³⁶ Cl for denudation rates of karst landform	Limestone	The Univ. of Tokyo	38
³⁶ Cl in meteorite	Meteorite	Tokyo Metro. Univ.	8
Development of the chemical procedure for sulfur reduction	Environmental samples (soil)	Univ. of Tsukuba	32
³⁶ Cl-AMS research and development	KN Standard sample	Univ. of Tsukuba	13
³⁶ Cl standard	KN Standard sample	-	90
¹⁴ C-AMS			
¹⁴ C-AMS for an efficiency test	Standard sample	Univ. of Tsukuba	5
³² Si-AMS			
³² Si-AMS research and development	SiO ₂	Univ. of Tsukuba	2

³⁶Cl-AMS

The performance of ³⁶Cl AMS was improved in AMS technique and system, such as a sample preparation technique, upgrade of the ion source and a new data acquisition system. Beam currents of ³⁵Cl⁻ and ³⁷Cl⁻ were able to be measured by the multi-Faraday cup set to the low energy side with a PC control system. Typical beam current of ³⁵Cl⁻ was 10 μA. ³⁶Cl¹⁴⁺ with the energy of 100 MeV was detected by a gas ΔE-E detector.

For ³⁶Cl AMS, the standard deviation of the fluctuation for the ³⁶Cl/Cl ratio is within ± 2 %, and the

¹ Radiation Science Center, High Energy Accelerator Research Organization

² Micro Analysis Laboratory, Tandem Accelerator, The University of Tokyo

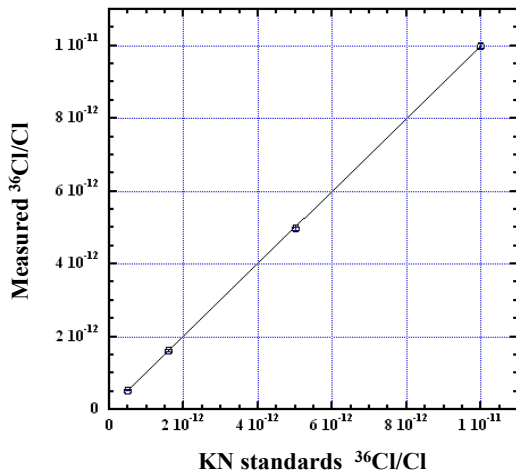


Fig. 1 Linearity of the measured $^{36}\text{Cl}/\text{Cl}$ ratios for the KN standard.

effective detection limit is better than 5×10^{-15} . In the year of 2007, we changed the standard reference sample to the KN standard^[2] provided by Prof. Nishiizumi, UC Berkeley, instead of the internal standard sample. Fig. 1 shows the linearity of the measured $^{36}\text{Cl}/\text{Cl}$ ratios for the KN standard ($^{36}\text{Cl}/\text{C}=1.00 \times 10^{-11}$, 5.00×10^{-12} , 1.60×10^{-12} and 5.00×10^{-13}) for 5 minutes measurements with 4 times. The measured data was normalized by the standard of $^{36}\text{Cl}/\text{C} = 1.00 \times 10^{-11}$. The result shows a good linearity with the statistical error of $\pm 1-2\%$.

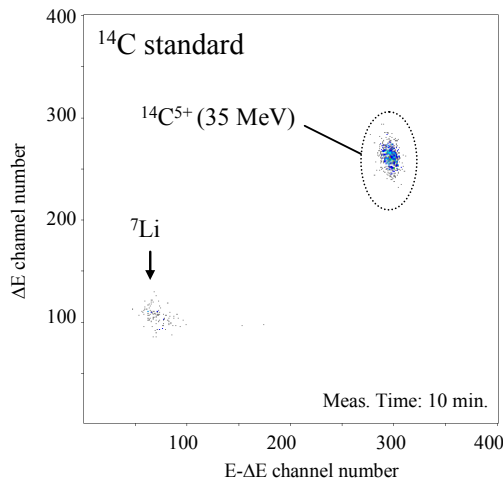


Fig. 2 $^{14}\text{C}^{5+}$ (35 MeV) spectrum of the standard sample.

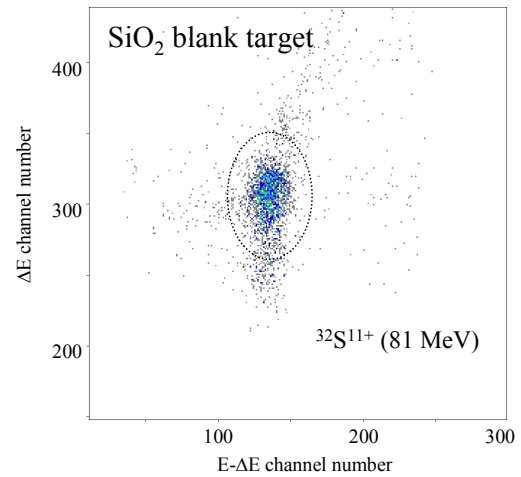


Fig. 3 Spectrum of the SiO_2 blank target.

^{14}C -AMS

We examined the performance of ^{14}C AMS. The terminal voltage was selected at 7 MV, and 35 MeV $^{14}\text{C}^{4+}$ was accelerated with a pilot beam of $^7\text{Li}_2$. After the 2nd stripper foil, 35 MeV $^{14}\text{C}^{5+}$ was detected by the gas ΔE -E detector. Fig. 2 shows the $^{14}\text{C}^{5+}$ spectrum for the standard sample. The measurement precision was approximately $\pm 5\%$.

^{32}Si -AMS

We checked the beam transport for ^{32}Si AMS by using the pure SiO_2 sample. The terminal voltage was selected at 9 MV, and the pilot beam of $^{16}\text{O}_2$ was used to stabilize the terminal voltage. $^{32}\text{Si}^{8+}$ and $^{16}\text{O}^{4+}$ had same mass energy product (ME/q^2) of 40.5 MeV amu. After the 2nd stripper foil, $^{32}\text{Si}^{8+}$ was changed to $^{32}\text{Si}^{11+}$. The transmission of $^{28}\text{Si}^{8+}$ with $\text{ME}/q^2 = 40.5$ MeV amu was 24.6 % for the AMS system. Fig. 3 shows the spectrum for the pure SiO_2 target as a blank sample. Isobaric interference of $^{32}\text{S}^{11+}$ was strongly appeared on the spectrum. Next step, the performance of ^{32}Si AMS will be examined by the standard sample.

References

- [1] K. Sasa et al., Nucl. Instrum. Methods Phys. Res. B259 (2007) 41-46.
- [2] P. Sharma et al., Nucl. Instrum. Methods Phys. Res. B52 (1990) 410-415.

1.3 Developments of ERCS hydrogen analysis

T. Komatsubara, K. Sasa, D. Sekiba, S. Ishii, Y. Yamato, K. Ebisu, T. Kawamata and M. Kurosawa

In order to improve precision and accuracy several developments have been performed for the Elastic Recoil Coincidence Spectrometry (ERCS) hydrogen analysis.

For the calibration of hydrogen content Mylar films are used as the reference material. However, long period of irradiation causes damage of the Mylar films to reduce scattering yields. Hydrogen in the films could be expelled by the atomic collisions of the beam irradiation. In order to estimate the reduction of the yield the damage cross section σ were measured. The damage cross section σ can be defined as

$$Y = Y_0 e^{-\sigma\phi}$$

where ϕ denotes fluence which is a ratio between number of irradiated particles and area of the irradiation. Y and Y_0 describe a scattering yield and its initial value.

Figure 1 shows measured results of damage cross sections by changing beam current. Mylar film of 2.5 micro m thick is irradiated by 20 MeV proton beam. Measured data are rather scattered, however, they remain in the range 0.4-0.9 Mb for the different beam current. An average of the damage cross section is evaluated to be 0.66 ± 0.06 Mb at 20 MeV.

Figure 2 shows energy dependence of the damage cross section. Calculated values by Kinchin-Pease model[2] are shown by a solid line where the cross section is proportional to inverse of the irradiation energy.

In the measurement of ERCS hydrogen analysis, depth profile is one of the advantages of this method. In order to improve quality of the depth profile, systematical measurements of the depth resolution were carried out.

For the target materials, thin foils of SiO₂, Al, Cu, and W were irradiated. The measured results are shown in Fig. 3 where the bombarding energy of the proton beam was 20 MeV. In this figure, detector resolution is subtracted. In Fig.3, a solid line shows Bohr value;

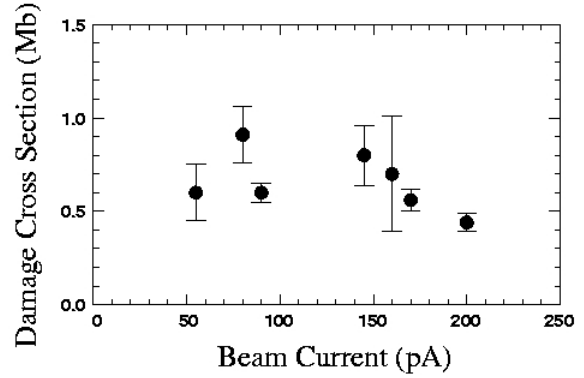


Fig. 1. Damage cross section depending on a beam current at an irradiation energy of 20 MeV.

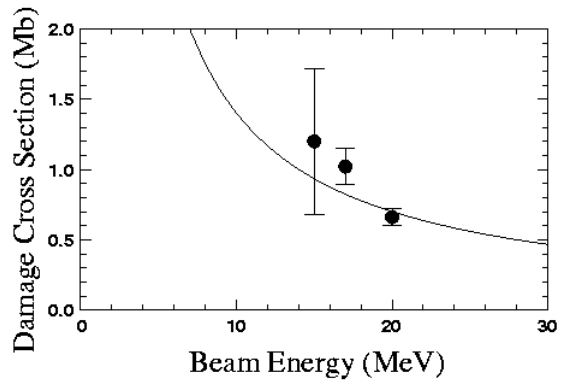


Fig. 2. Damage cross section as a function of beam energy. Solid line shows calculated values by Kinchin-Pease model[2].

$$FWHM = 2\sqrt{2\ln 2} \frac{1}{4\pi\epsilon_0} \sqrt{4\pi z^2 e^4 \frac{Z}{A} N_a x}$$

where z denotes atomic number of the projectile, A and Z are mass and atomic numbers for target, x is thickness of the target film in (g/m²) and N_a denotes Avogadro constant. The measured results are well reproduced by the Bohr values except for the W.

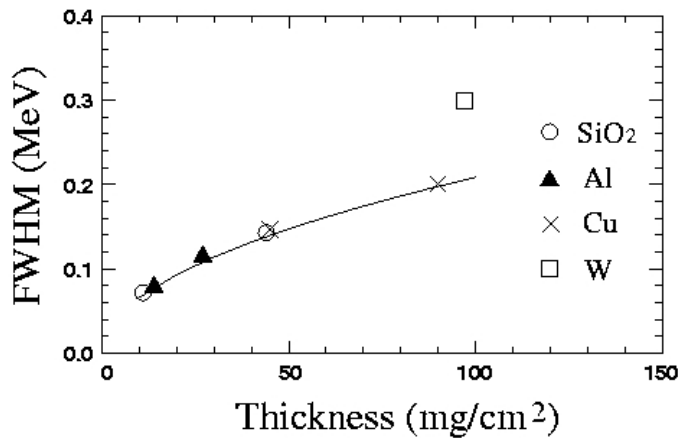


Fig. 3. Straggling for SiO₂, Al, Cu and W. Bohr values are shown by the solid line.

In order to reduce edge scattering as background of spectra, detector slits were modified. Single slit system has been changed to be double slit system. Consequence of the modification, edge scattering is reduced to be about 70%. Geometry of the new slit system is shown in Table 1. Detection solid angle is determined by the first slit in right detector to be 35.1 msr.

Table 1 New slit system for ERCS coincidence detectors.

	Diameter(mm)	Distance(mm)	Solid angle (msr)
Right-1	5.6	26.5	35.1
Right-2	10	38	54.3
Left-1	10	26.5	111.8
Left-2	14	38	106.6

References

- [1] T. Komatsubara *et al.* Nucl. Instr. and Meth. B251 (2006) 237
- [2] P. Reichart *et al.* Nucl. Instr. and Meth. B197 (2002)134

2.

NUCLEAR PHYSICS

2.1 Production of radioactive nuclear beam of ^8Li and its in-flight identification

K. Y. Hara, A. Ozawa, Y. Hashizume, S. Igarashi, Y. Ito, T. Moriguchi, K. Ogawa, Y. Tagishi, K. Yamaguchi, and Y. Yasuda

A radioactive nuclear beam of ^8Li (half life $t_{1/2}=838$ ms) was produced at UTTAC by using a transfer reaction. A 40-MeV $^7\text{Li}^{3+}$ beam from the tandem accelerator was irradiated on a CD_2 target with a thickness of about 1 mg/cm^2 . The intensity of $^7\text{Li}^{3+}$ beam was ~ 100 nA. As shown in the inset of Fig.1, the target was located at downstream of an analyzer magnet. The $^8\text{Li}^{3+}$ beam ejected at a forward angle by the $\text{D}(^7\text{Li}, ^8\text{Li})\text{p}$ reaction was transported to the beam line of F-course in the first experimental room. The energy of $^8\text{Li}^{3+}$ beam is estimated at about 38 MeV by taking account of the kinematics of the $\text{D}(^7\text{Li}, ^8\text{Li})\text{p}$ reaction and the energy loss in the CD_2 target. In order to separate the secondary beam from the primary beam, a Q-Q-D-Q-Q transport system which consists of a switching magnet and 2 doublet quadrupole magnets was used (see the inset of Fig.1), where Q and D stand for quadrupole magnet and dipole magnet, respectively.

Figure 1 shows an experimental setup at F-course for in-flight particle identification. A Q-D-Q magnetic spectrograph at zero degree to the beam line was set with a magnetic rigidity (B ρ) for the $^8\text{Li}^{3+}$ beam. The beam was measured with 2 parallel-plate avalanche counters (PPAC's) and a telescope of ΔE -E Si solid-state detectors (SSD's). For the calibration of the detectors, the faint beams of $^7\text{Li}^{3+}$ from the accelerator at 34 and 40 MeV were also transported.

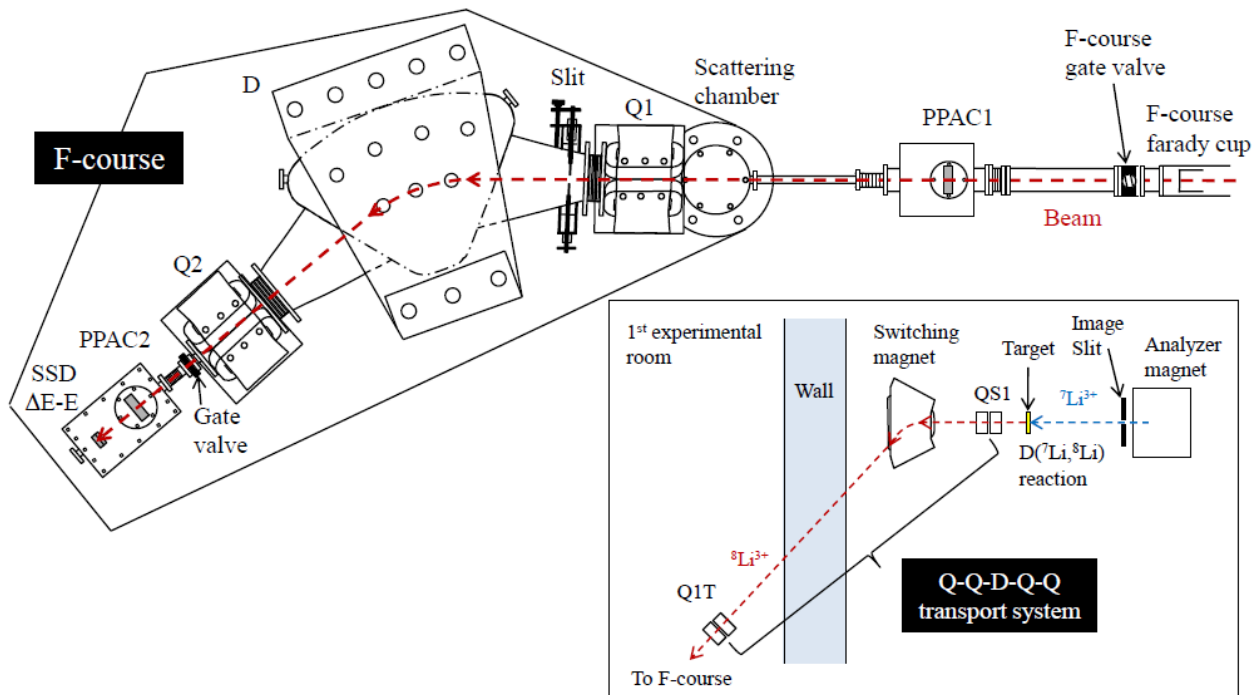


Fig.1: Schematic views of the experimental setup in F-course and the Q-Q-D-Q-Q transport system.

PPAC consists of three plates; cathode (X), anode, and cathode (Y) [1]. The beam was monitored by the

counting rates of the anodes signals and the two-dimensional positions derived from the charge-division signals of the cathodes. The start and the stop signals for TOF measurements were obtained from the anodes of PPAC1 and PPAC2, respectively. The flight path between PPAC1 and PPAC2 is ~ 4 m. The full width at half maximum in the TOF spectrum is 6 ns (Fig. 2 (a)). The ΔE -SSD with a thickness of 50 μm and E-SSD with a thickness of 300 μm were used in the energy loss and total energy measurements, respectively. These energy spectra are shown in Fig. 2(b) and 2(c). Peaks in the low-energy part show pedestal; where the beam do not hit both SSD's, while the coincidence events of PPAC1 and PPAC2 are used as the trigger signals for the data acquisition. The typical counting rates are 1 kcps at PPAC1 and 100 cps at PPAC2. In contrast, the counting rates of SSD's are very low (~ 10 cps). The rate of PPAC1 is reasonable in comparison with one estimated from the cross section of the $D(^7\text{Li}, ^8\text{Li})p$ reaction. The counting rates of PPAC2 and SSD's could be improved with the optimization of beam transport.

The two-dimensional scatter plot of the energy loss in ΔE -SSD versus TOF is shown in Fig. 2(d). For in-flight particle identification, the results of calculations for $^7\text{Li}^{2+}$, $^7\text{Li}^{3+}$, and $^8\text{Li}^{3+}$ with the same B ρ are also plotted as the triangle, square, and circle, respectively, in the figure, where we calculated the energy loss in the detectors and the TOF by assuming the 38-MeV incident energy of the $^8\text{Li}^{3+}$ beam at upstream of PPAC1. The locus in Fig. 2(d) is in agreement with the estimation for $^8\text{Li}^{3+}$ and is nearly free from the contamination of the primary beam. In addition to the above B ρ -TOF- ΔE method, we confirm the particle identification by using the Fig. 2(e) that shows the two-dimensional scatter plot of the energy loss in ΔE -SSD versus the summed energy in its ΔE -E telescope. The calculations are presented in the Fig. 2(e) as well as Fig. 2(d).

The present results show the present setup allows in-flight identification for radioactive nuclear beam. Therefore it may be possible to measure, for example, total reaction cross section at the present energy. The particle identification is indispensable in these experiments. Further developments are required.

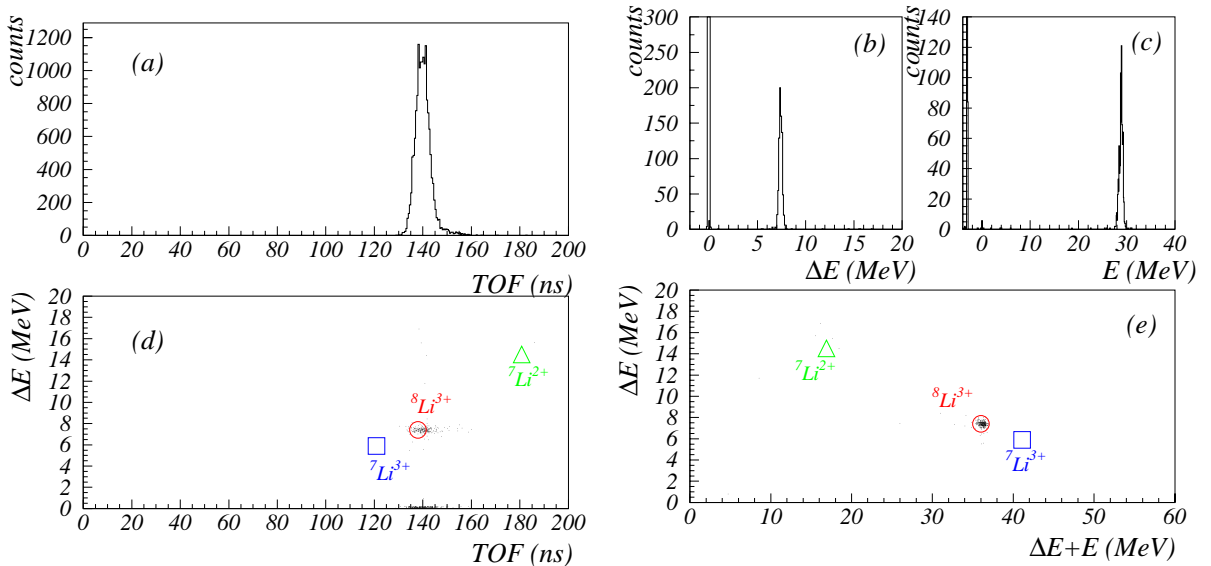


Fig.2: (a) TOF spectrum between PPAC1 and PPAC2, (b) energy spectrum of ΔE -SSD, (c) energy spectrum of E-SSD, (d)(e) two-dimensional scatter plots for particle identification (see text for details).

References

- [1] H. Kumagai *et al.*, Nucl. Instr. and Meth. A **470** (2001) 562.

2.2 $^{118}\text{Sn}(\text{d},\text{p})$ reaction in search for Coulomb stripping of deuteron. V

M.Iijima, Y.Aoki and A.Ozawa

Coulomb stripping of deuterons were proposed by Oppenheimer and Phillips in the 1930s [1]. To elucidate its mechanism, we measured $^{118}\text{Sn}(\text{d},\text{p}_{0,1,2})$ reactions at $E_d = 3.2 \sim 6.0\text{MeV}$ [2]. The residual nucleus ^{119}Sn has its first and second excited states at $E_x = 23.9\text{keV}$ and 89.5keV . We tried to measure only $^{118}\text{Sn}(\text{d},\text{p}_0)$ at the beginning of the experiment. Later it was found difficult at our detector resolution to separate $^{118}\text{Sn}(\text{d},\text{p}_0)$ reaction from (d,p_1) and (d,p_2) reactions. Thus the deduced experimental cross sections are for the sum of the three reactions, which are denoted in Fig.1 as circles with errors in it. Theoretical $\frac{d\sigma}{d\Omega}$ for the reactions are calculated by DWBA and CDCC(d,p). As for the difference between DWBA and CDCC(d,p), it is explained in terms of transition matrices. The matrix element for A(d,p)B reaction [3] is given by:

$$T(\text{d},\text{p}) = \langle \chi_p^{(-)} \Phi_B | V_{\text{np}} + V_{\text{pA}} - U_{\text{pB}} | \Psi_{\text{dA}}^{(+)} \rangle \quad (1)$$

where Φ_B is the internal wave function for the residual nucleus, $\chi_p^{(-)}$ is the distorted wave under optical potential U_{pB} , and $\Psi_{\text{dA}}^{(+)}$ is the full wave function of the incident channel. In CDCC(d,p) calculations $(V_{\text{pA}} - U_{\text{pB}})$ is neglected and $\Psi_{\text{dA}}^{(+)}$ is replaced by the product of CDCC wave function $\Psi_{\text{CDCC}}^{(+)}$ and internal wave function Φ_A .

$$T(\text{CDCC}(\text{d},\text{p})) = \langle \chi_p^{(-)} \Phi_B | V_{\text{np}} | \Psi_{\text{CDCC}}^{(+)} \Phi_A \rangle \quad (2)$$

In DWBA $\Psi_{\text{dA}}^{(+)}$ is replaced by $\chi_d^{(+)} \Phi_A$, where $\chi_d^{(+)}$ is the initial state distorted wave function under optical potential U_{dA} .

$$T(\text{DWBA}) = \langle \chi_p^{(-)} \Phi_B | V_{\text{np}} | \chi_d^{(+)} \Phi_A \rangle \quad (3)$$

Finite range DWBA calculations [4] are performed for $^{118}\text{Sn}(\text{d},\text{p}_0)$, (d,p_1) and (d,p_2) reactions respectively. We need to get the sum of the DWBA cross sections $\left(\frac{d\sigma}{d\Omega}\right)_{(\text{d},\text{p}_0)}$, $\left(\frac{d\sigma}{d\Omega}\right)_{(\text{d},\text{p}_1)}$ and $\left(\frac{d\sigma}{d\Omega}\right)_{(\text{d},\text{p}_2)}$ to fit the experimental $\frac{d\sigma}{d\Omega}$.

$$\frac{d\sigma}{d\Omega} = S_0 \left(\frac{d\sigma}{d\Omega}\right)_{(\text{d},\text{p}_0)} + S_1 \left(\frac{d\sigma}{d\Omega}\right)_{(\text{d},\text{p}_1)} + S_2 \left(\frac{d\sigma}{d\Omega}\right)_{(\text{d},\text{p}_2)} \quad (4)$$

S_0 , S_1 and S_2 are the spectroscopic factors for (d,p_0) , (d,p_1) and (d,p_2) reactions respectively. We set $(S_0, S_1, S_2) = (1.55, 0, 0)$ to examine the (d,p_0) contribution. S_0 is adjusted to the value to normalize the DWBA cross sections at $E_d = 6.0\text{MeV}$. Thus obtained DWBA cross sections are shown in lines of Fig.1. It is clear that the experimental cross sections are underestimated at $E_d = 3.2$ and 3.5MeV . We also set $(S_0, S_1, S_2) = (0, 1.77, 0)$ and $(0, 0, 5.8)$ to check (d,p_1) and (d,p_2) contributions respectively. The values $S_1 = 1.77$ and $S_2 = 5.8$ are chosen to normalize DWBA cross sections to those of experiments at $E_d = 6.0\text{MeV}$. In both cases there are underestimations at $E_d = 3.2$ and 3.5MeV . Thus it is clear from (4) that it would be difficult to reproduce the experimental cross sections at $E_d = 3.2$ and 3.5MeV by DWBA calculations.

We performed CDCC(d,p) calculations at $E_d = 6.0\text{MeV}$ and obtained $\frac{d\sigma}{d\Omega}$ with and without the Coulomb break-up (CBU) contributions. We take $(S_0, S_1, S_2) = (1.0, 0, 0)$ in (4) and compare $\frac{d\sigma}{d\Omega}$ with the DWBA calculation (Fig.2). When we get the values of $\frac{d\sigma}{d\Omega}$ at $\theta_{\text{CM}} = 130^\circ$, the ratios of CDCC(d,p) cross sections

to that of DWBA are 0.99 without CBU and 0.87 with CBU. These CDCC(d,p) calculations still requires improvements of parameters and we are now working on it.

References

- [1] J. R. Oppenheimer and M. Phillips, Phys. Rev. **48**, 500(1935).
- [2] M.Iijima, T.Ishikawa, D.Inomata and Y.Aoki, UTTAC Annual Report **76**, 12(2007)
- [3] M.Iijima, Y.Aoki, A.Ozawa and N.Okumura, Nucl. Phys. A **793**, 79(2007).
- [4] M. Igarashi, Computer code TWFNR, private communication. Full manual/source list can be downloaded from <http://www.tac.tsukuba.ac.jp/~yaoki>.

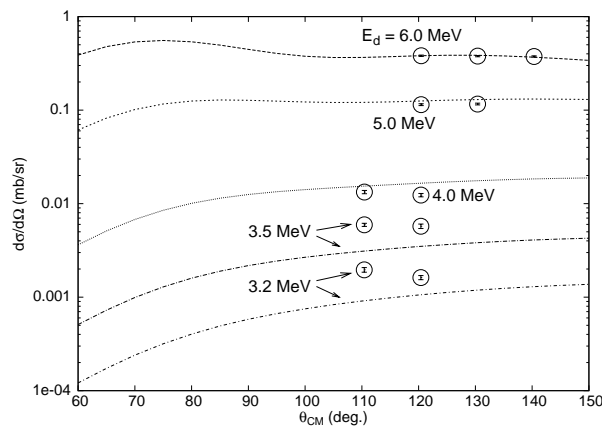


Fig. 1. Experimental and calculated cross sections

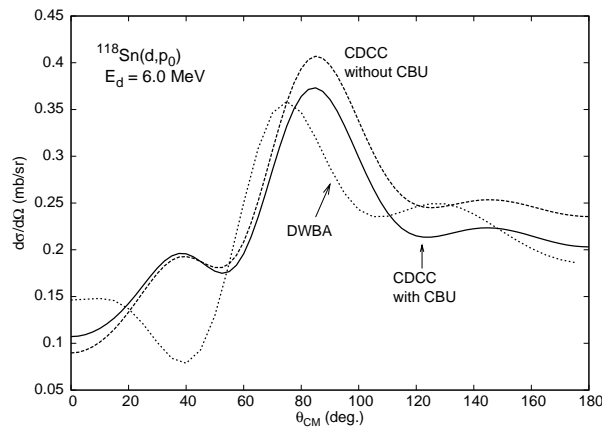


Fig. 2. Comparison of DWBA and CDCC(d,p) cross sections

2.3 Measurement of the time response in Hybrid Photo Detector II

T. Moriguchi, Y. Hashizume, T. Hoya, K. Ogawa, Y. Yasuda, K. Hara and A. Ozawa

The Isochronous Storage Ring at RIKEN RI Beam Factory (RIBF) is designed to measure mass of unstable nuclei. The purpose of the research is nuclear synthesis in neutron rich side with r-process, where it is predicted that Uranium was synthesized. However, the prediction is not proved due to difficulty of production of such neutron rich nuclei. RIBF will be able to produce many unstable nuclei that we had never reached in the past. The precise mass of these unstable nuclei is expected to understand the path of the r-process.

We determine the mass by measuring the cyclotron frequency which can be measured by TOF (Time Of Flight) of the nuclei inside the Storage Ring. In order to determine mass precisely ($\delta m/m \sim 10^{-6}$), TOF detectors need to have high timing resolution ($< 100\text{ps}$).

We started to develop a Hybrid Photo Detector (HPD) as TOF detectors with high timing resolution. In 2006, we measured the timing resolution of HPD (HAMAMATSU R7110U-07) at University of Tsukuba Tandem Accelerator Complex (UTTAC) [1]. The timing resolution of the previous HPD is worse than that of the Photo Multiplier Tube (PMT, HAMAMATSU R4998). In 2007, we tested a high speed HPD (HS-HPD, HAMAMATSU R10467U-06) whose Avalanche Diode was developed newly to be very low capacitance. The photocathode of HS-HPD was fabricated on a plano-concave faceplate of $\phi 8$ mm to adjust the transit time of electrons to be equal over the photocathode. HS-HPD as shown in Figure 1 has fast time response and small transit time spread (see Table 1).

Table 1. Specifications of HPD [2][3].

		HPD	High Speed HPD
Photocathode	Material	Multialkali	Bialkali
	Effective Area [mm]	$\phi 8$	$\phi 8$
	Max High Voltage [kV]	-8.5	-8.5
Avalanche Diode	Capacitance [pF]	140	3.4
	Max Bias Voltage [V]	+155	+405
Electron Bombarded Gain		1200	1500
Avalanche Gain		50	90
Rise Time [ns]		1.1	0.4
Fall Time [ns]		14.8	0.4
Transit Time Spread [ps]		277	47

The experiment was performed at 1F course with Q-D-Q magnet in the 12UD tandem accelerator of UTTAC using 60MeV carbon beam with the same setup in previous [1]. Figure 2 shows a schematic view of the experimental setup. We measured the timing resolution of two different types of HS-HPDs, Positive HS-HPD (P-HPD) and Negative HS-HPD (N-HPD) in Fig. 2. Both HS-HPDs have almost same specifications except the difference of polarity of output signals. We also tested PMT2 in order to compare the time response with the HPD. In the experiment, we changed only the detectors, keeping PMT1 with a

plastic scintillator. The detectors were located in a box to shield the light. The trigger signal was made by the coincidence with two signals from both side detectors.

Figure 3 shows typical pulse shapes from P-HPD and PMT1. The pulse from N-HPD was also the same as that from P-HPD except for the polarity. Rise time of HS-HPD was 4ns, this value was the same as that of PMT. However, the pulse height of HS-HPD was less than PMT since the gain of HS-HPD is smaller than PMT by two orders of magnitude. During the measurement of the timing resolution, the pulse height of HS-HPD was amplified by using amplifiers (ORTEC AN302/N). Table 2 shows the results of the timing resolution of HS-HPD and PMT2. AMP in Table 2 means the number of using amplifiers. According to Table 2, larger pulse height becomes better timing resolution. HS-HPD achieved the better timing resolution than that of the previous HPD [1]. However, the timing resolution of HS-HPD was worse than that of PMT2.

In summary, we measured the timing resolution of HS-HPD with 60MeV carbon beam in UTTAC. Comparing the results of HS-HPD with those of the previous HPD, the rise time was faster and the timing resolution was better. However, the timing resolution of HS-HPD was worse than that of PMT.



Fig. 1. The high speed HPD (HAMAMATSU R10467U-06).

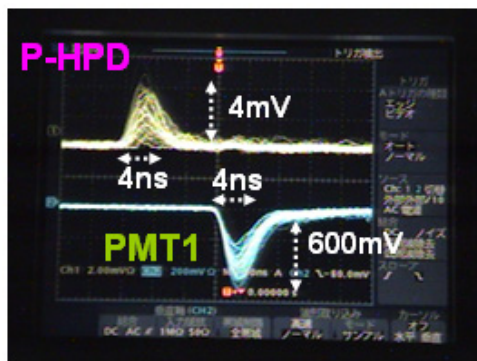


Fig. 3. Typical pulse shapes for P-HPD and PMT1, respectively.

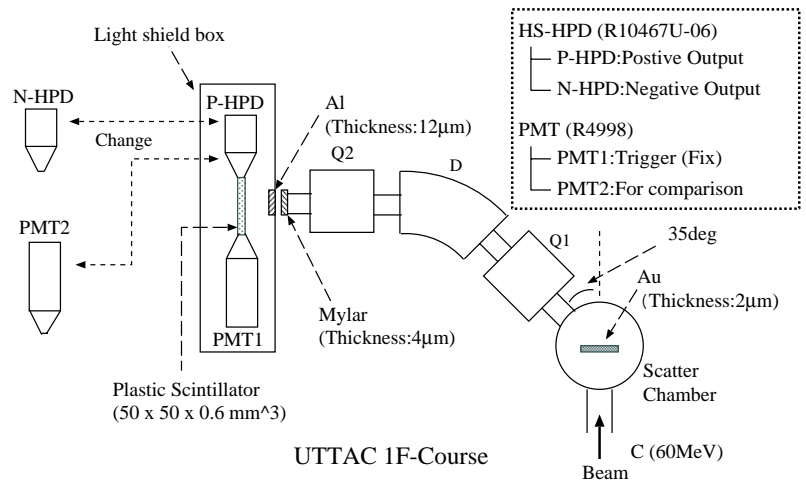


Fig. 2. Schematic view of the experimental setup.

Table 2. The results of the timing resolution [ns].

AMP	0	2	3	4
P-HPD	-	590 ± 3	453 ± 4	389 ± 3
N-HPD	-	603 ± 3	434 ± 3	390 ± 2
PMT2	249 ± 1	-	-	-

References

- [1] T. Moriguchi *et al.*, UTTAC Annual Report 2006, UTTAC-76 (2007) 14.
- [2] Hamamatsu Photonics K.K., Electron Tube Division, technical note of R7110U series (2001).
- [3] Hamamatsu Photonics K.K., Electron Tube Division, technical note of R10467 series (2006).

2.4 Study of nuclear synthesis of ^{26}Al by gamma ray spectroscopy

T. Komatsubara, K. Ebisu, T. Kawamata, A. Ozawa, K. Hara, T. Moriguchi, Y. Hashizume, T. Shizuma*, T. Hayakawa* and S. Kubono[#]

* JAEA

[#] Tokyo University, CNS

Since observation of 1.809-MeV gamma rays by satellite gamma ray telescope has been reported[1], the astrophysical study of ^{26}Al is very important for nuclear synthesis. The gamma ray is observed emitting from center of our galaxy. The Doppler shift of the observed gamma ray energy is consistent to the rotation of the galaxy. The ground state of the ^{26}Al is 5^+ and its half life is 7.2×10^4 year. The state decays into the 2^+ state of ^{26}Mg and emits the gamma ray from the 2^+ to 0^+ . If one considers that the half life is short compared to the period of the life of the galaxy, it can be understood that the nuclear synthesis should be active at present. Diehl estimated that the mass of the ^{26}Al is 2.8 solar in our galaxy and rate of super-nova is $1.9 \pm 1.1 / 100$ years[1]. The origin of the ^{26}Al is still unknown. Massive star, Wolf Rayet star, nova or super-nova are candidates of the production location.

The nucleus ^{26}Al can be created by $^{25}\text{Mg}(p,\gamma)$ reaction. However there is bypass reaction sequence $^{25}\text{Al}(p,\gamma)^{26}\text{Si}(\beta,\nu)^{26\text{m}}\text{Al}(\beta,\nu)$ which emits no gamma ray of 1.809 MeV. The bypass sequence is considered to be proceeded via 3^+ resonance state in ^{26}Si which is not established yet. The purpose of this study is to investigate nuclear levels in ^{26}Si for the estimation of production rate of ^{26}Al .

By using reaction analysis, there are several researches to investigate nuclear levels in ^{26}Si . Badayan reported observation of levels above proton threshold by (p,t) reaction[2]. Caggiano used ($^3\text{He},^6\text{He}$) reaction to populate the levels[3]. Parpottas investigated by ($^3\text{He},n$) reaction measuring emitting neutron spectra[4]. Recently, Seweryniak studied excited states in ^{26}Si by using GAMMA SPHERE[5] observing 1^+ state at 5677-keV.

In order to investigate level structure in ^{26}Si , in-beam gamma ray spectroscopy was performed at UTTAC by using Ge detectors. The excited states of the ^{26}Si were populated by the nuclear reaction $^{24}\text{Mg}(^3\text{He},n)^{26}\text{Si}$. The ^3He beam of 10 MeV was irradiated on a natural Mg target. Gamma-gamma coincidence measurements were performed by using three Ge detectors. Relative efficiencies of the Ge detectors are 140%, 70% and 50%. Two neutron detectors were also employed for the test experiment of neutron-gamma coincidence measurements.

As a result of the analysis of the coincidence measurements, level scheme of ^{26}Si is shown in Fig. 1. A new level is found at 5886-keV which is above proton threshold. The newly found level is fed into the first 2^+ and the second 2^+ states by emitting 3100- and 4089-keV gamma rays, respectively. If one compares the nuclear structure with mirror nucleus ^{26}Mg [6], spin of this level can be assigned other than 3^+ because strong feeding has been observed from the third 3^+ to the second 3^+ in the ^{26}Mg .

References

- [1] R. Diehl, H. Halloin, K. Kretschmer, G.G. Lichti, V. Schönfelder, A.W. Strong, A. Kienlin, W. Wang, P. Jean, J. Knödlseeder, J.P. Roques, G. Weidenspointner, S. Schanne, D.H. Hartmann, C. Winkler, C. Wunderer, *Nature* 439 (2006) 45
- [2] D.W. Bardayan, J.C. Blackmon, A.E. Champagne, A.K. Dummer, T. Davinson, U. Greife, D. Hill, C. Iliadis, B.A. Johnson, R.L. Kozub, C.S. Lee, M.S. Smith, P.J. Woods, *Phys. Rev. C* 65 (2002) 032801(R)
- [3] J.A. Caggiano, W.B. Smith, R. Lewis, P.D. Parker, D.W. Visser, J.P. Greene, K.E. Rehm, D.W. Bardayan, A.E. Champagne, *Phys. Rev. C* 65 (2002) 055801
- [4] Y. Parpottas, S. M. Grimes, S. Al-Quraishi, C.R. Brune, T.N. Massey, J.E. Oldendick, A. Salas, T. Wheeler, *Phys. Rev. C* 70 (2004) 065805
- [5] D. Seweryniak, P.J. Woods, M.P. Carpenter, T. Davinson, R.V.F. Janssens, D.G. Jenkins, T. Lauritsen, C.J. Lister, J. Shergur, S. Sinha, A. Woehr, *Phys. Rev. C* 75 (2007) 062801(R)
- [6] P.M. Endt, *Nucl. Phys. A* 633 (1998) 1

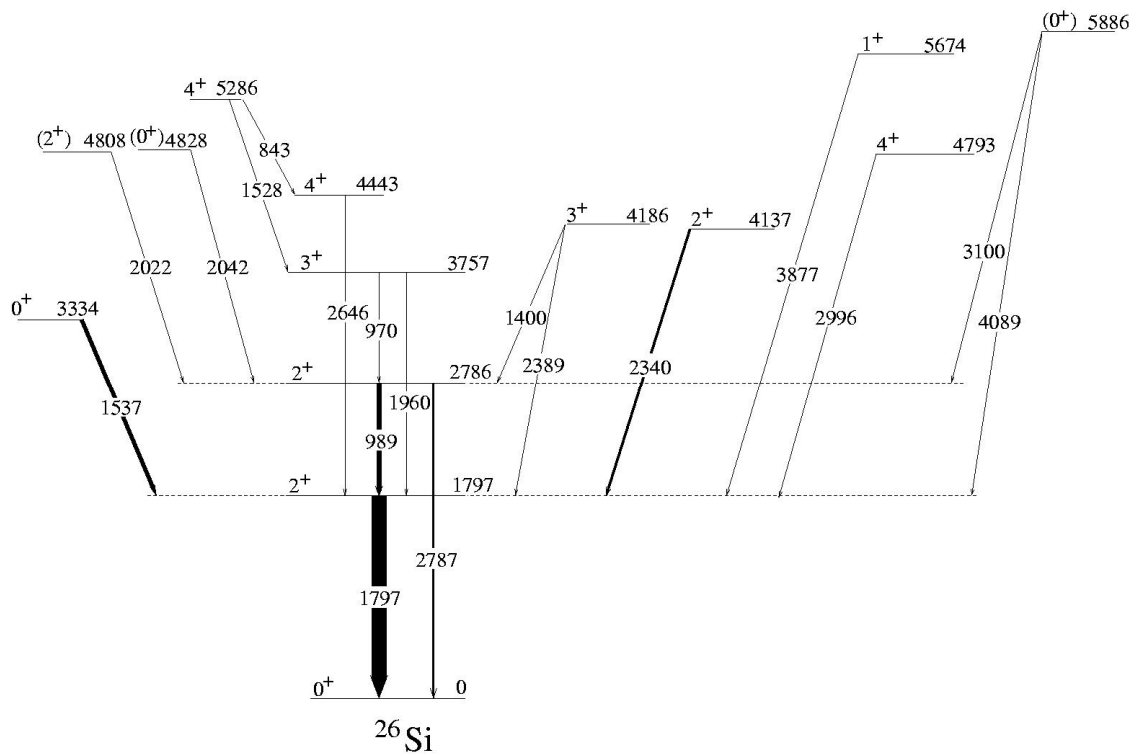


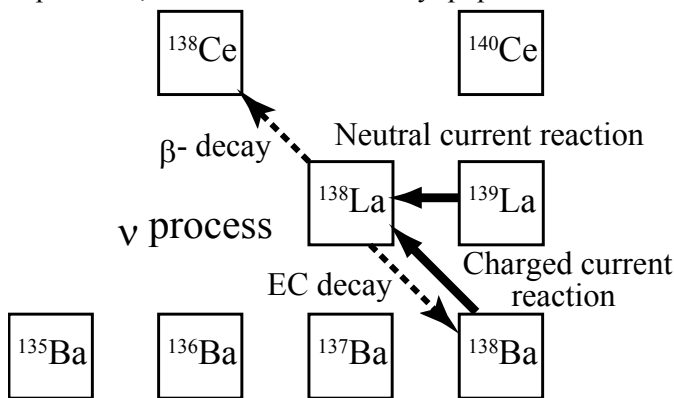
Fig.1 Level structure of ^{26}Si .

2.5 Nuclear structure of supernova neutrino-process isotope ^{138}La

T. Hayakawa ^{1,2}, T. Komatsubara, T. Shizuma ¹

Rare odd-odd isotopes of ^{138}La and ^{180}Ta are grouped to p-nuclei [1]. As the origin of the two isotopes, a supernova neutrino-induced reaction nucleosynthesis (ν -process) was suggested [2]. The ν -process is of importance for studying neutrino spectra from the supernovae, and for discussing neutrino oscillation [3,4]. Among many heavy elements, only two isotopes of ^{138}La and ^{180}Ta are considered to be synthesized primarily by the ν -process but ^{180}Ta is also considered to be produced by the s-process. The solar abundance of ^{138}La was quantitatively explained by the ν -process in theoretical calculations [3,5]. Recently, Hayakawa et al. proposed ^{138}La as a nuclear cosmochronometer for measuring the time elapsed from a neutrino-window driven supernova explosion [6]. Therefore, ^{138}La is a key isotope for understanding the ν -process. Information of low spin excited states in ^{138}La are of importance for theoretical calculation of neutrino-induced reaction rate (see Fig. 1) but the details of the low spin states have not been studied well experimentally. Here we study the nuclear structure of ^{138}La by using in-beam gamma-ray spectroscopy technique with a (p, n) reaction.

Excited states in ^{138}La were populated by a $^{138}\text{Ba}(p, n)^{138}\text{La}$ reaction. The proton beam of an energy of 10 MeV was provided by the tandem accelerator at University of Tsukuba. Compressed BaCO_3 powder was used as a target with a thickness of about 70 mg/cm^2 . ^{138}Ba was enriched to about 99%. In the present experiment, ^{138}La was dominantly populated since neutron evaporation channel is dominant in this



reaction and we used the enriched target. The γ -rays from the excited states were detected with three HPGe detectors. The evaporated neutrons were detected by a liquid scintillator. The efficiencies of the HPGe detectors were about 50-70% relative to a 3 in. \times 3 in. NaI detector. Typical energy resolution was 2.6 keV at 1.3 MeV. We obtained γ - γ and γ -n coincidence data, leading information of nuclear structure of ^{138}La .

Fig.1. Nuclear synthesis flow around ^{138}La

References

- [1] T. Hayakawa, et al. to be published in *Astrophys. J* (2008).
- [2] S.E Woosley, et al., *Astrophys. J.* 356, 272 (1990).
- [3] A. Heger, et al., *Phys. Lett. B* 606, 258 (2005).
- [4] T. Yoshida, et al., *Phys. Rev. Lett.*, 96, 091101 (2006).
- [5] A. Byelikov, et al., *Phys. Rev. Lett.* 98, 082501 (2007).
- [6] T. Hayakawa, et al., to be published in *Phys. Rev. C* (2008).

¹ Japan Atomic Energy Agency

² National Astronomical Observatory

3.

MATERIALS AND CLUSTER SCIENCE

3.1 Synthesis of elongated and oriented gold nanorods in silica by irradiation of swift heavy ion

K. Awazu¹, X. Wang¹, M. Fujimaki¹, J.Tominaga¹, H.Aiba², Y.Ohki², T. Komatsubara

It has been reported that elongated Au nanoparticles oriented parallel to each other can be synthesized in SiO₂ by ion irradiation.[1] Our aim was to elucidate the mechanism for this elongation. We prepared Au nanoparticles with various diameters from 10 to 80 nm in a SiO₂ matrix. Figure 1 shows a cross-sectional transmission electron micrograph of SiO₂-embedded Au nanoparticles after irradiation by 110-MeV Br¹⁰⁺ at a fluence of $1 \times 10^{14} \text{ cm}^{-2}$. Note that elongation of Au nanoparticles with a small radius was larger than that of Au nanoparticles with a large radius. These experimental results are discussed in the framework of a thermal spike model of Au nanorods with a radius of 5 or 10 nm embedded in SiO₂. As shown in Figure 2 (a), the lattice temperature [2] exceeds the melting temperatures of both SiO₂ and Au for 100 ns after one 110-MeV Br¹⁰⁺ ion has passed through the middle of an Au nanorod of radius of 5 nm. In contrast, with the 10-nm Au rod shown in Figure 2 (b), neither the rod nor the SiO₂ is melted by 110-MeV Br¹⁰⁺. We conclude that dependence of the elongation of the Au nanoparticles on particle size can be explained in terms of the thermal spike model.

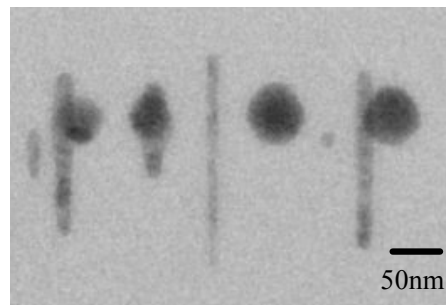


Fig.1. Cross-sectional TEM image of Au nanoparticles of various sizes in SiO₂ irradiated with 110-MeV Br¹⁰⁺.

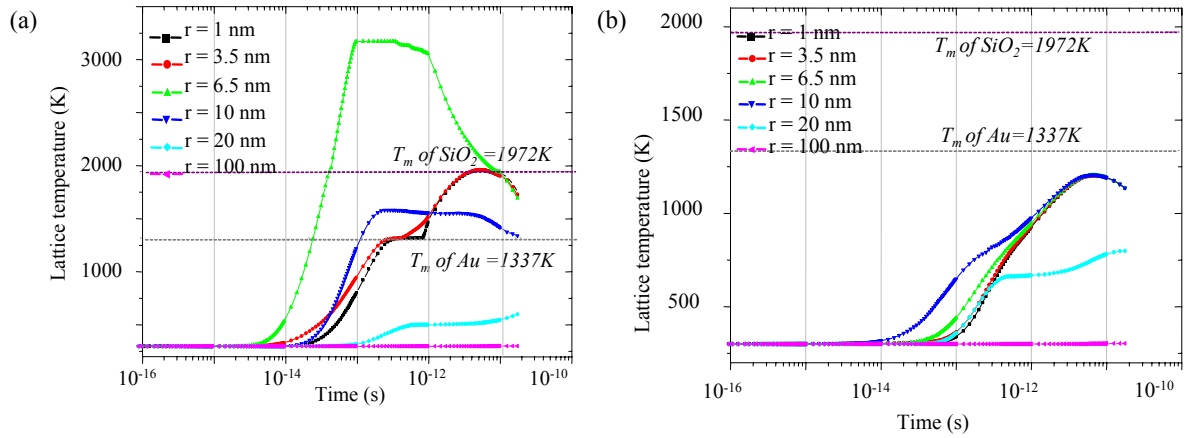


Fig.2. The simulated evolution of the electronic temperature versus time at various distances (1, 3.5, 6.5, 10, 20, and 100 nm) from the ion path when a 110 MeV Br^{10+} ion penetrates the center of a gold particle embedded in SiO_2 . The radii of the Au nanoparticles are 5 nm (a) and 10 nm (b). The beam electronic energy loss rate is assumed to be $S_e = 9.203$ keV/nm. The initial temperature of the sample is 300 K.

References

- [1] S. Roorda et al., Adv. Mater. 16 (2004) 235.
- [2] M. Toulemonde et al., Nucl. Instr. and Meth. B166-167 (2000) 903.

3.2 Characterization of Er-doped GaN by heavy ion RBS

T. Waki, Y. Kaku, S. Tomita, A. Uedono, Shaoqiang Chen, K. Akimoto, and H. Kudo

Rutherford backscattering spectroscopy (RBS) using fast heavy ions can provide high mass-resolution analysis of heavy elements embedded in the surface layers of materials. Actually, this has been applied to the characterization of Er-doped GaN with interest on the crystal quality and the lattice site of Er atoms in GaN. Such structural information is of essential importance in electronic device applications.

The GaN samples were 0.8- μm -thick Er-doped GaN grown on (0001) sapphire substrates by gas-source MBE using NH_3 as the nitrogen source [1]. The RBS measurements were carried out using 30-MeV O^{5+} obtained from a 12MV tandem accelerator, and also using 1.6-MeV He^+ for comparison of the mass resolution. The three-axis goniometer used for channeling incidence conditions was remote-controlled under the pressure of $\sim 3 \times 10^{-6}$ Pa.

Figure 1 compares the nonchanneling RBS spectra for the two beams, which were obtained for the same sample. The spectra for Ga and the doped Er can be separated for 30-MeV O^{5+} , while they are seriously overlapped for 1.6-MeV He^+ , demonstrating the high mass-resolution of heavy ion RBS.

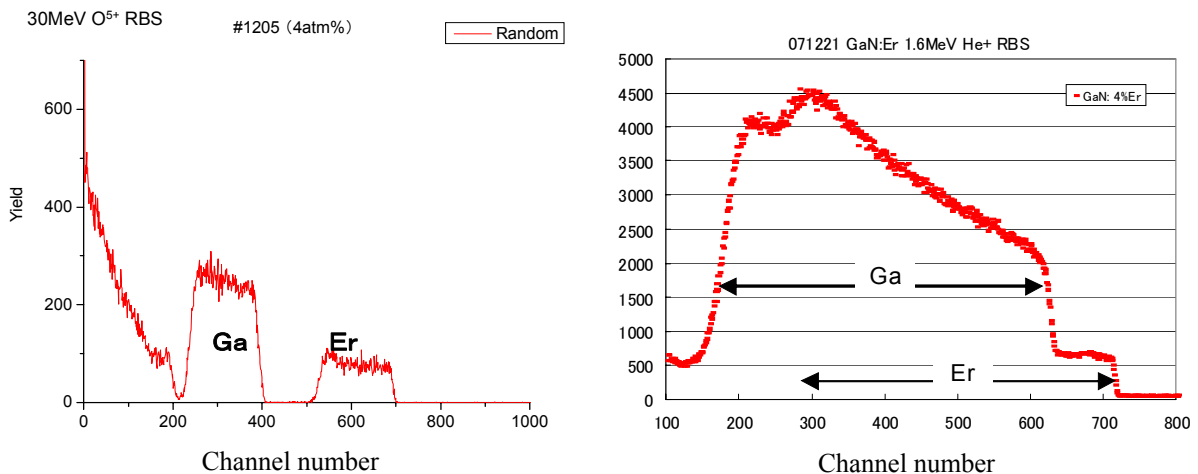


Fig.1 Comparison of the RBS spectra for 30-MeV O^{5+} and 1.6-MeV He^+ .

Figure 2 shows the results for RBS-channeling measurements using 30-MeV O^{5+} . In Fig. 2(a), the minimum yield which is a measure of the crystal quality is as large as ~ 0.75 even for Er doping of 1at%. This is contrast to the observed minimum yield of ~ 0.01 for nondoped GaN. The tilt-angle dependence of the RBS yield from the substrate Ga and the doped Er is shown in Fig. 2(b). A comparison of the angular dips for Er and Ga indicates that, on the average, $\sim 75\%$ Er atoms occupy substitutional sites. The rest 25% should correspond to small displacement from the substitutional sites. Determination of the site of 25% Er requires further information about the behavior of Er in an imperfect GaN lattice.

Furthermore, we have found an increase of Er concentration near the GaN/substrate interface. The stress due to the lattice mismatch near the interface might be relaxed by the concentrated Er which provides a

bond-length of Er-N which is different from Ga-N. Thus, Er is likely to accumulate near the interface and would result in the introduction of vacancy-type defects which have been observed recently by using a monoenergetic positron beam [2].

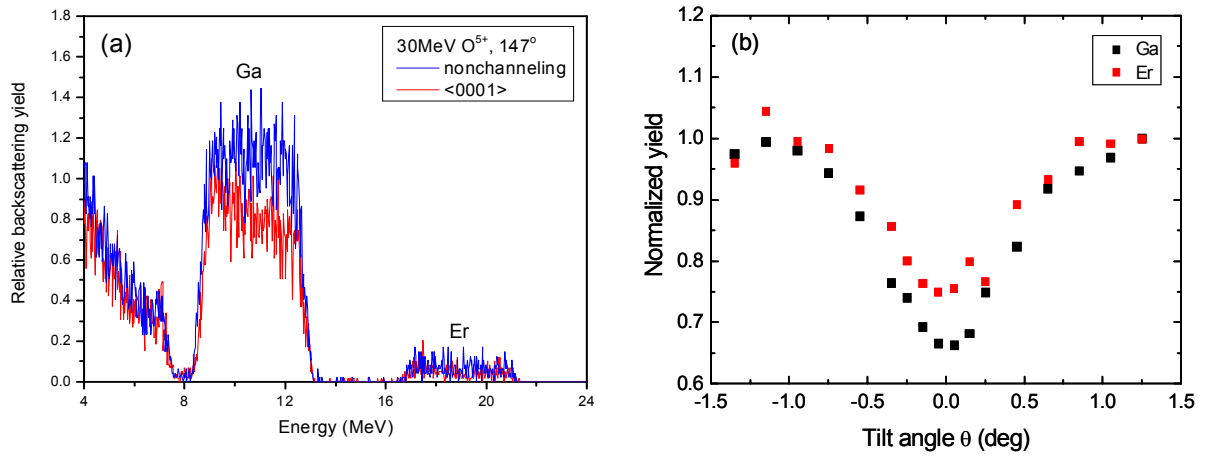


Fig. 2 (a) RBS-channeling spectra of 1at%-Er doped GaN, epitaxially grown on sapphire.
 (b) Tilt-angle dependence of the RBS yield near $\langle 0001 \rangle$.

References

- [1] S. Morishima, T. Maruyama, K. Akimoto, J. Crystal Growth **209**, 378 (2000).
- [2] A. Uedono et al., accepted for publication.

3.3 Dependence of the vicinage effect on interatomic spacing of carbon clusters

M. Murakami, S. Tomita, K. Shiba, S. Ishii, K. Sasa and H. Kudo

When fast molecular ions are incident on a solid, the energy loss per atom is different from that of single atomic ions. This is known as ‘‘vicinage effect’’. In the case of 0.5MeV/atom C_n^+ ($n=1\sim 4$) clusters, the energy loss for cluster ions is lower than that of atomic ion. The results are quantitatively understood by considering the interference of electrons scattered by individual atoms. The vicinage effect should become weaker with increasing the foil thickness because the interatomic distance within the injected cluster ion increases as the ion penetrates deeper. In this work, we investigate the dependence of the vicinage effect in the energy loss of carbon clusters on the foil thickness.

Schematic experimental setup is shown in Fig.1. A thin carbon foil was mounted on one side of the double frame which underwent metronomic motion together with other empty frame. The projectiles

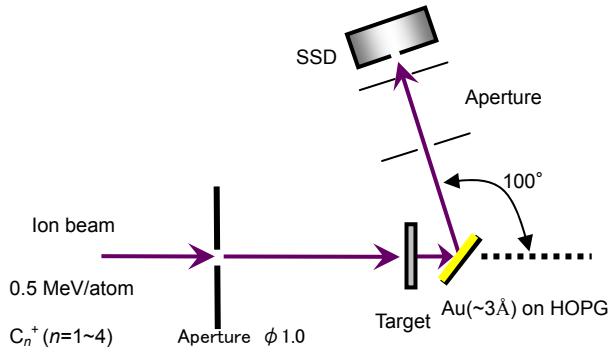


Fig.1. Schematic view of the experimental setup in the scattering chamber

transmitted either through the foil or the empty frame hit a thin Au target placed at just downstream of the device. The energy of the scattered carbon atoms by the target was measured with particle detector (SSD) at a backward angle of 100° . The energy of C_n^+ was 0.5 MeV/atom. The thicknesses of the carbon foil were 3.3 and $14.2 \mu\text{g}/\text{cm}^2$. Atomic distances inside the foil were estimated from the coulomb explosion of C_2^+ as 1.7 and 5.3 \AA for 3.3 and $14.2 \mu\text{g}/\text{cm}^2$, respectively.

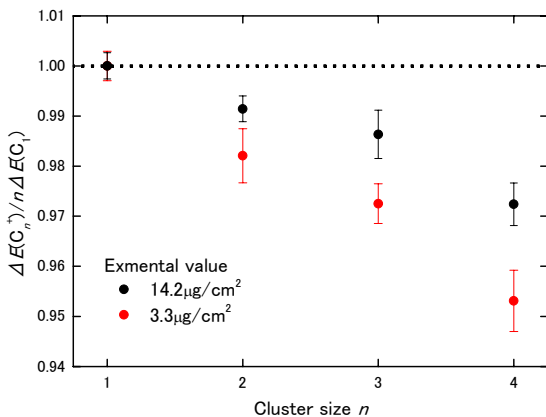


Fig.2. The energy loss per atom of 0.5MeV/atom C_n^+

The ratios of the observed energy loss to that of atomic ions are shown in Fig.2. As seen in Fig. 2, the energy-loss ratios for C_4^+ are 0.953 and 0.972 for 3.3 and $14.2 \mu\text{g}/\text{cm}^2$, respectively. If the vicinage effect disappears at a depth of $3.3 \mu\text{g}/\text{cm}^2$, the ratio of the observed energy loss for $14.2 \mu\text{g}/\text{cm}^2$ should be $3.3 \times 0.953 + (14.2 - 3.3) \times 1 / 14.2 = 0.989$. However, the observed value is 0.972. From this difference, we can conclude that the vicinage effect surely remains at a depth of $3.3 \mu\text{g}/\text{cm}^2$.

3.4 Point defects in Er-doped GaN probed by means of positron annihilation

H. Nakamori, A. Uedono, C. Shaoqiang, S. Jongwon, K. Ito, N. Honda, S. Tomita, K. Akimoto, H. Kudo, and S. Ishibashi¹

Optical properties of Er-doped GaN have been extensively studied due to their potential in device applications. The emission efficiency of Er-doped GaN, however, is very low and it was reported that intensities of photo luminescence (PL) are strongly influenced by the presence of a special distribution of point defects and dislocations [1]. Hence, a fundamental understanding of the behavior of point defects is very important to effectively utilize optical devices based on RE-doped GaN. In the present study, we probed vacancy-type defects in Er-doped GaN using positron annihilation spectroscopy (PAS) to investigate the relationship between such defects and the emission intensity.

The samples were 0.8- μm -thick Er-doped GaN grown on (0001) sapphire substrates by gas-source MBE using NH_3 as the nitrogen source. Details of the growth method are given elsewhere [2]. Before growth, the substrate was nitridated under an NH_3 pressure of 5×10^{-3} Pa for 10 min at 940°C . The substrate temperature was kept at 700°C during the growth. 3.5- μm -thick undoped GaN was also fabricated using growth conditions similar to those described above. PL measurements were done using an Argon laser (488 nm) at 77K. The structural properties of the films were evaluated by x-ray diffraction (XRD) using Cu $K\alpha_1$ and $K\alpha_2$ radiation. The Er concentrations [Er] and their depth distributions were measured by Rutherford back scattering (RBS) using 30-MeV O^{5+} obtained from a 12 MV tandem-accelerator. With a monoenergetic positron beam, the Doppler broadening spectra of the annihilation radiation were measured as a function of the incident positron energy for samples with an Er concentration between 0.3 at.% and 6.0 at.%. The resultant changes in the spectra are characterized by the S parameter, defined as the number of annihilation events over the energy range of $511 \text{ keV} \pm \Delta E_\gamma$ (where $\Delta E_\gamma = 0.76 \text{ keV}$) around the center of the peak and by the W parameter, which is calculated from the tail of the peak, in the range of $3.4 \text{ keV} \leq |\Delta E_\gamma| \leq 6.8 \text{ keV}$. In general, the characteristic value of S (W) for the annihilation of positrons trapped by vacancy-type defects is larger (smaller) than that for positrons annihilated from the free-state.

In Fig. 1, the S values as a function of incident positron energy E for each sample were shown. The S value increased with increasing Er-concentration ([Er] \leq 3.3 at.%), suggesting the introduction of vacancy-type defects due to Er incorporation. For Er-doped GaN with [Er] = 6.0 at.%, however, the S value was smaller than that for the sample with [Er] = 3.3 at.%. This sample was observed degradation of the crystallinity from XRD measurements. Therefore, it was considered that a positron could detect vacancies related to precipitates or metastable phases in the amorphous sample. The Er depth distributions were shown in Fig. 2 and agreed well with that of vacancy-type defects, suggesting Er was accumulated near the GaN/substrate interface where vacancy-type defects were introduced.

¹ Research Institute for Computational Sciences, National Institute of Advanced Industrial Science and Technology, Tsukuba, Ibaraki, 305-8568, Japan

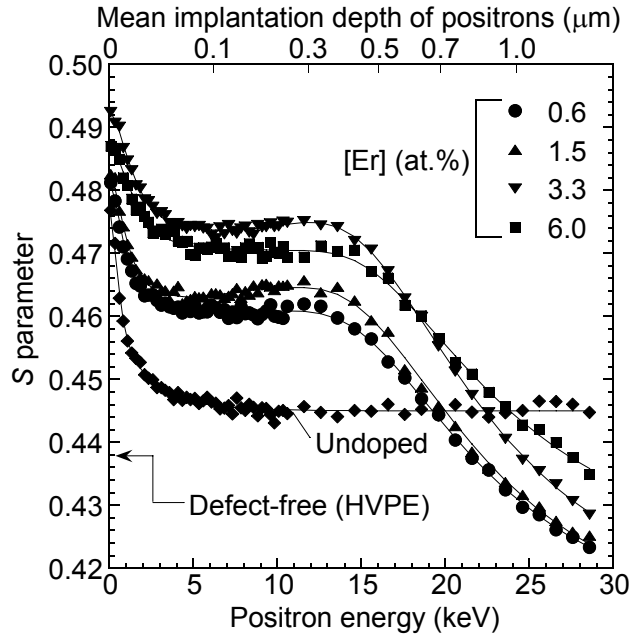


Fig. 1 S as a function of incident positron energy E for Er-doped GaN with $[\text{Er}] = 0.3\text{-}6.0$ at.%. The result for undoped GaN is also shown.

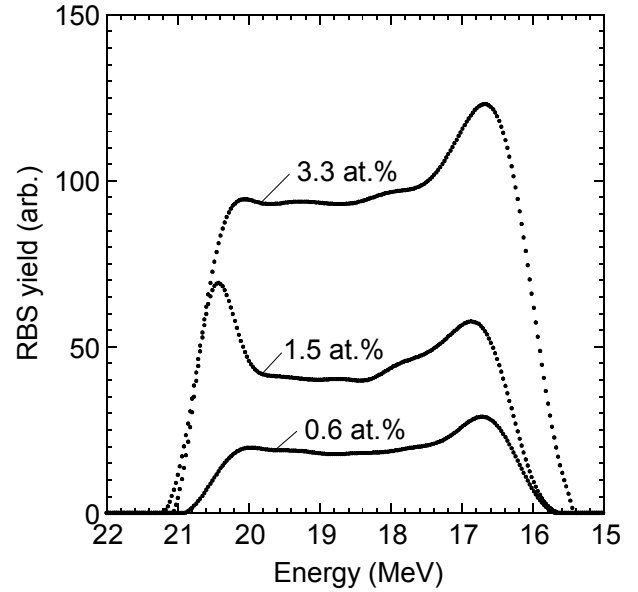


Fig. 2 RBS random spectra corresponding to the depth distributions of Er in GaN with Er concentrations of 0.6, 1.5, and 3.3 at.%.

We have also obtained a clear correlation between the point defects and the intensity of the intra- $4f$ transitions of Er. By the analysis of detail using S - W relationship and first-principles calculation [3, 4], it was found that the major defect species detected by positron was identified as a Ga-vacancy (V_{Ga}) for the undoped and Er-doped GaN with $[\text{Er}] = 0.3\text{-}1.5$ at.% and its concentration increased with increasing Er concentration; the V_{Ga} concentration reached $3 \times 10^{18} \text{ cm}^{-3}$ at $[\text{Er}] = 1.5$ at.%. For the sample with $[\text{Er}] = 3.3$ at.%, the maximum integrated intensity of PL was observed, while the introduction of additional vacancies such as divacancies started at this doping concentration.

In conclusion, we can suggest that defect engineering to control the defect species and their concentrations while preserving a highly crystalline GaN matrix is one key to increasing the emission rate of the intra- $4f$ shell transitions from a RE metal.

References

- [1] A. Ishizumi, J. Sawahata, K. Akimoto, Y. Kanemitsu, Appl. Phys. Lett. **89**, 191908 (2006).
- [2] S. Morishima, T. Maruyama, K. Akimoto, J. Crystal Growth **209**, 378 (2000).
- [3] A. Uedono, K. Ito, H. Nakamori, K. Mori, Y. Nakano, T. Kachi, S. Ishibashi, T. Ohdaira, and R. Suzuki, J. Appl. Phys. **102**, 084505 (2007).
- [4] S. Ishibashi, Materials Science Forum **445-446**, 401 (2004).

3.5 Rutherford backscattering spectroscopy on Pt-adsorbed HOPG surface

D. Sekiba, T. Kondo, J.P. Oh, S. Ishii, H. Kudo, and J. Nakamura

Recently the Pt cluster evaporated on the highly oriented pyrolytic graphite (HOPG) has attracted much attention as a model system of an electrode in low-temperature fuel cells. It has been known that the catalytic activity of the Pt cluster on HOPG strongly depends on the structure in atomic scale, which changes by catalytic treatment: evaporation condition, temperature and atmosphere during the catalytic reactions. In particular, the catalytic activity of Pt cluster after increasing the temperature of the HOPG substrate has been controversial. We have made experiments of temperature program desorption (TPD) spectroscopy of CO on Pt/HOPG. It has been found that the Pt cluster after one cycle of TPD measurement no longer has the catalytic activity to adsorb the CO molecule again. This indicates that the system of Pt/HOPG was drastically changed due to the increase of temperature. A similar change of the Pt/HOPG system were reported in terms of the electronic and morphologic structures by means of X-ray photoemission spectroscopy (XPS). A.R. Howells et al. reported the binding energy shift of the Pt4f state at ~ -71 eV from Fermi level toward the lower binding energy with increasing the substrate temperature up to 500 K, meanwhile the intensity of the Pt4f photoelectrons decreased continuously with increasing the temperature. They observed also the change of the surface morphology due to the heating treatment by scanning tunneling microscope (STM). The Pt island, which has dendritic structure, disappeared and only unclear protrusions were observed.

There are some possibilities to interpret the catalytic activity loss of the Pt cluster after the heating treatment. One is that the electronic structure of Pt is changed due to the chemical bonds with the surrounding carbon atoms, etc., and another extreme possibility is that the Pt atom desorbed from the HOPG surface. Both cases do not conflict with the results of the XPS measurements. In other words, the XPS measurements following the change of the photoelectron intensity cannot distinguish whether the Pt atoms exist in subsurface region of HOPS or the Pt atoms are really removed from the system. To elucidate this problem, we made Rutherford backscattering spectroscopy (RBS) measurements, which can estimate the absolute amount of the Pt atoms in the subsurface region as well as on the surface.

We mainly prepared four samples of Pt/HOPG: clean HOPG, 30 min. Pt-evaporated HOPG, 30 min. Pt-evaporated HOPG with a subsequent annealing up to 700 K, and finally 40 min. Pt-evaporated HOPG. The RBS measurements were done at the beam line C in Tandetron accelerator. The 1.6 MeV He ion (~ 2.5 nA) was used, and the backscattered ions were detected by a solid state detector (SSD) at the angle of 153 degree with respect to the beam incident direction. The collected charge of He ion was set at 5×10^{-7} C on target for a spectrum.

Figure 1 shows the RBS spectra taken on the four samples. We can see the steep edge at ~ 190 channel indicating the HOPG substrate and the position of this edge is common among all the samples. No impurity heavier than carbon was detected on the clean HOPG sample. On the Pt-evaporated samples we can see distinct peak at ~ 725 channel indicating the existence of Pt atoms. The estimated coverages of Pt on the 30min Pt-evaporated, 30 min. Pt-evaporated and annealed and 40 min. Pt-evaporated HOPG are

0.08 ML (mono-layer), 0.17 ML and 0.29 ML, respectively. It is noteworthy that an intense peak corresponding to Pt was observed also on the sample annealed up to 700 K, so that the heating treatment does not remove the Pt atoms from the substrate. This means that the loss of the catalytic activity of Pt due to the heating treatment is caused by the change of chemical state of Pt, for example, the migration into the subsurface region. Another indication by RBS results is fluctuation of the Pt evaporation rate during the sample preparation. The Pt coverage determined by RBS is not exactly proportional to the evaporation duration. The improvement of evaporation method will enable us to make more precise experiments on this system.

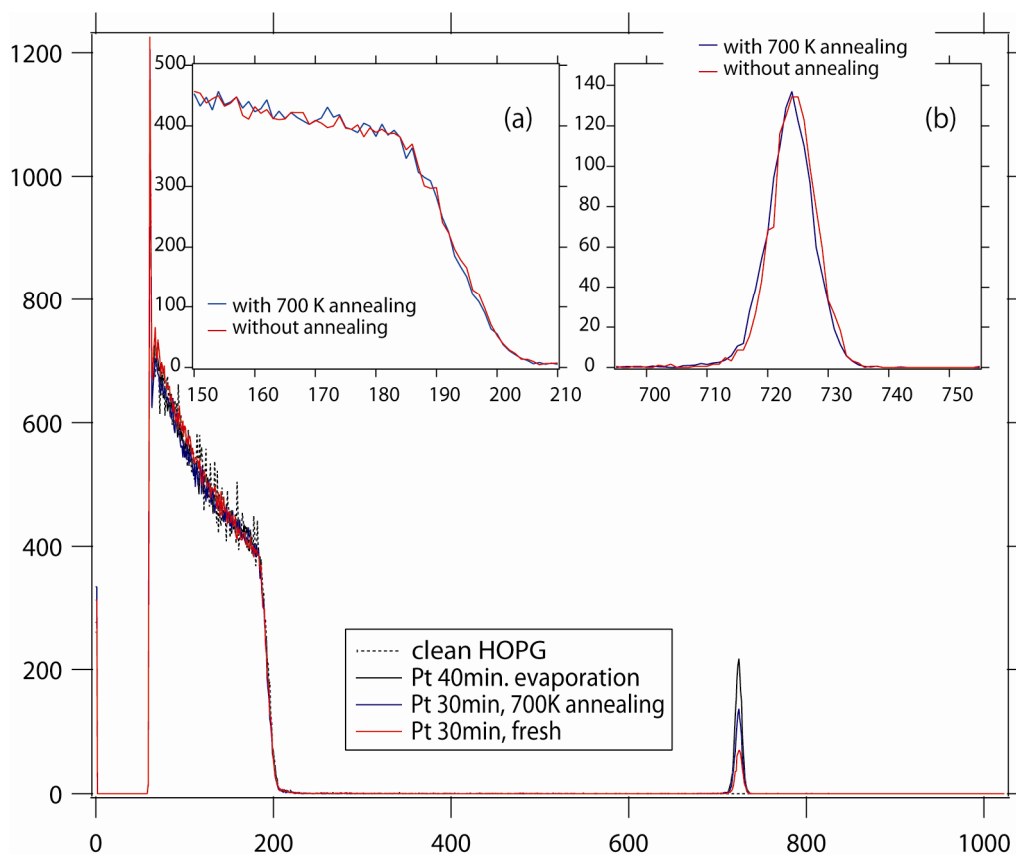


Figure 1: RBS spectra taken on the clean HOPG, 30 min. Pt-evaporated HOPG, 30 min. Pt-evaporated HOPG with a subsequent annealing up to 700 K, and finally 40 min. Pt-evaporated HOPG. The insets (a) and (b) compare the positions of edge and peak corresponding to the HOPG substrate and Pt, respectively. The edge position of HOPG is identical on both samples, while the Pt peak position is slightly different indicating that the change of the environment surrounding the Pt atoms, though the difference is still within the margin of error in the experiments.

References

- [1] G. Zhang, D. Yang, E. Sacher, *J. Phys. Chem. C* 2007, 111, 565 – 570.
- [2] A.R. Howells, L. Hung, G.S. Chottiner, D.A. Scherson, *Solid State Ionics*, 2002, 150, 53 – 62.

3.6 Mössbauer study of sub-micron sized Fe₃O₄ particles and NH₃ nitrized particles

M. Minagawa, H. Yanagihara, E. Kita and M. Kishimoto¹

Recently iron nitrides attract much attention again as new magnetic materials because of their fine magnetic properties and low environmental loads[1]. However iron nitride compounds are categorized as interstitial alloys, we have hardly ever obtained bulk samples so we have gained little information about their essential physical properties. Therefore, we have synthesized iron nitride particles that have sub-micron diameter and determined their phases with X-ray diffraction (XRD) study and the Mössbauer spectroscopy.

Fe₃O₄ particles with spherical shape and 130 nm in diameter were used as a starting material. An XRD pattern for the starting material is shown in Fig. 1(a). The oxide powder was reduced in H₂ flow at 400 °C for 2.5 hour and we obtained grayish powder (Fig.1(b)). After reduction, the powder was nitrized in NH₃ flow at 230 °C for 24 hour (Fig.1(c)). From the XRD pattern, the particles consist mostly of γ'-Fe₄N phase and small amount of ε-Fe₃N phase was detected. In order to increase the portion of γ' phase, a successive nitridding technique was developed. The nitridded particles were H₂ reduced for shorter period and was followed by NH₃ nitridding. The procedure and corresponding XRD were summarized in Table I.

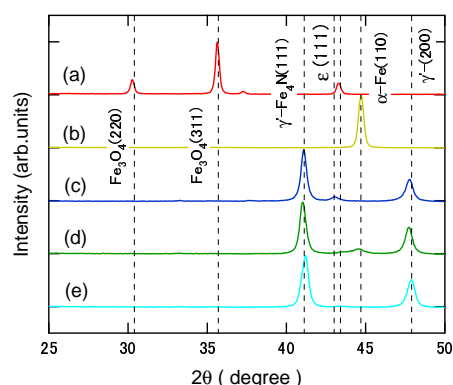


Fig. 1. Powder XRD patterns of the samples in nitridation processes

sample	nitriding temp	nitriding time	reducing temp	reducing time	re-nitriding temp	re-nitriding time	XRD pattern
(a)			starting material				Fig.1(a)
(b)			as reduced at 400°C				Fig.1(b)
(c)	230 °C	24 h					Fig.1(c)
(d)	↑	↑	230 °C	1.0 h			Fig.1(d)
(e)	↑	↑	↑	1.75 h	205 °C	18 h	Fig.1(e)

Table 1. Reducing and nitriding conditions for the successive nitriding technique

At the stage of sample(c), the ε-Fe₃N phase concentrated at the surface region and the annealing in

¹Hitachi Maxell, Ltd.

H₂ flow pulled out nitrogen atoms forming NH₃. Thus the surface became α -Fe. The most satisfactory condition was obtained with annealing in H₂ flow for 1.75 hour followed by nitriding again at 205 °C in NH₃ flow for 18 hour. An XRD pattern for the stage is shown in Fig.1(e) and it supports that the particles were mostly in a γ' -Fe₄N single phase. From those steps of samples, we picked up the samples (a), (b) and (e), and Mössbauer studies were carried out.

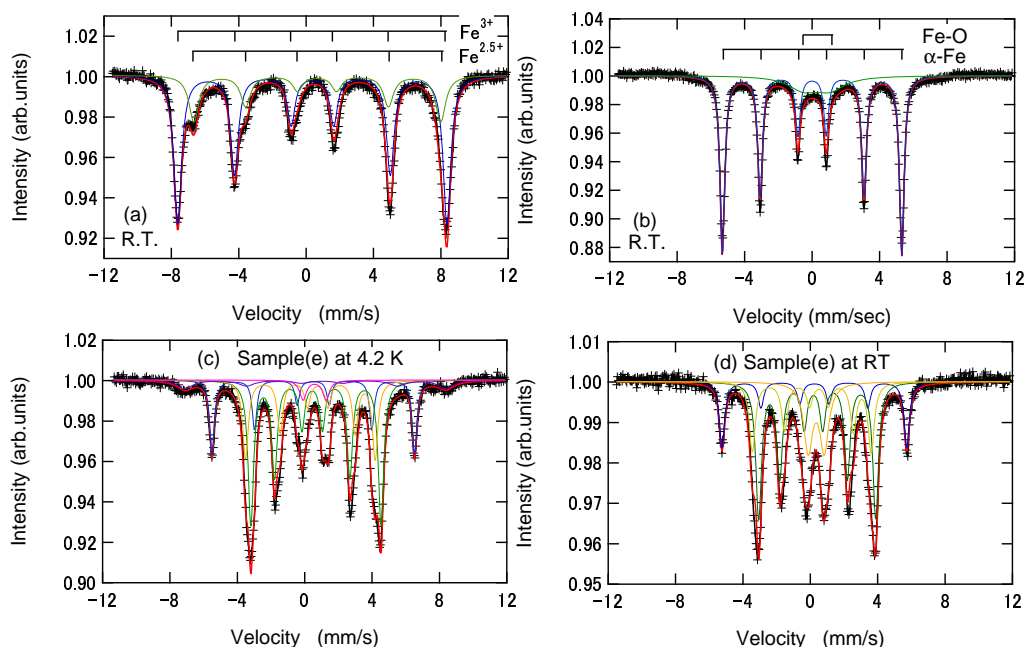


Fig. 2. Mössbauer spectrum of the samples in the nitridation processes

Mössbauer spectra for samples (a) and (b) recorded at room temperature are shown in Figs. 2 (a) and (b). The sample (e) was measured first at 4.2K in high vacuum, and after exposing in air, data were taken at room temperature (Figs. 2 (c) and (d)). The spectrum for the starting material (Fig.2(a)) shows that a fraction of Fe^{2.5+} and Fe³⁺ was reverted compared with that for stoichiometric Fe₃O₄. This result implies a presence of vacancies in Fe site. The spectrum for the reduced particles (Fig.2 (b)) was fitted to a subspectrum corresponding to α -Fe (81 %) and a doublet (19 %). The doublet may originate in surface oxides produced during the sample handling in the air. The thickness of the surface oxide is estimated to be 8.8 nm. We obtained 89 % of γ' -Fe₄N and oxide fraction of 11 % in the nitride sample (e) at 4.2K (Fig. 2(c)). The thickness of the surface oxide is about 5.0 nm. From the room temperature experiment after exposing the sample (e) in air, the fraction of γ' -Fe₄N decreased to 84 % and the fraction of iron oxide increased. The thickness of the surface oxide was about 7.5 nm.

In conclusion, we fabricated spherical sub-micron γ' -Fe₄N particles using the successive nitriding technique and proved that it was in an almost single phase with Mössbauer spectroscopy.

References

- [1] J. M. D. Coey and P. A. I. Smith, *J. Magn. Magn. Meter.*, **200**, 405-424 (1999).

3.7 Molecular dynamics calculation of water clusters

T.Ikuyama and I.Arai

We have carried out Molecular Dynamics(MD) calculation [1] for water cluster as a preliminary work for a study of hydrate cluster. In present study, we are interested in the structure of small water cluster $(\text{H}_2\text{O})_n$ ($n=2-9$) which gives a crucial knowledge for the study of hydrate cluster. In our MD calculation, a water molecule is treated as a rigid body consisting of three piont-like atoms, i.e., two hydrogen atoms and one oxygen atom. Actually, we have used SPC/E potential [2] as a two-body effective potential among water molecules.

The results are as follows. The dimer forms a linear hydrogen bond as expected (type-2). The trimer makes a triangular shape (type-3). The tetramer is a regular tetrahedron (type-4) which is formed by putting one extra water molecule above the mass center of type-3. The pentamer exhibits two types of structures. One is a triangular dipyramid (type5-1) and the other is a square pyramid (type5-2). The hexamer exhibits three types of structures. One is a regular octahedron (type6-1), the next is a cage (type6-2) and the last is a triangular prism (type6-3). The heptamer exhibits two types of structures. One is a prism shape with one triangular base and one rhombic base (type7-1) and the other is a pentagonal dipyramid (type7-2). The octamer exhibits two types of structures. One is a rhombic prism (type8-1) and the other is a hexagonal dipyramid (type8-2). The nonamer exhibits three types of structures. One is a threefold-stacked triangular prism (type9-1), the next is a cage consisting of a prism shape with one triangular base and one pentagonal base and one extra molecule on the top(type9-2) and the last is a cage consisting of a prism shape with one rhombic base and one trapezoidal base and one extra molecule in the midpoint of the trapezoidal base's long side(type9-3).

In the present study, the search for stable structures was made by hand without any efficient strategy. For further study of stable structures, more efficient approach such as genetic search should be introduced.

References

[1] F.Cleri and V.Rosato, Phys. Rev. B, 48, 22 (1993).

[2] H.J.C.Berendsen, J.R.Grigeria, and T.P.Straatsma, J. Phys. Chem. 91, 6269 (1987).

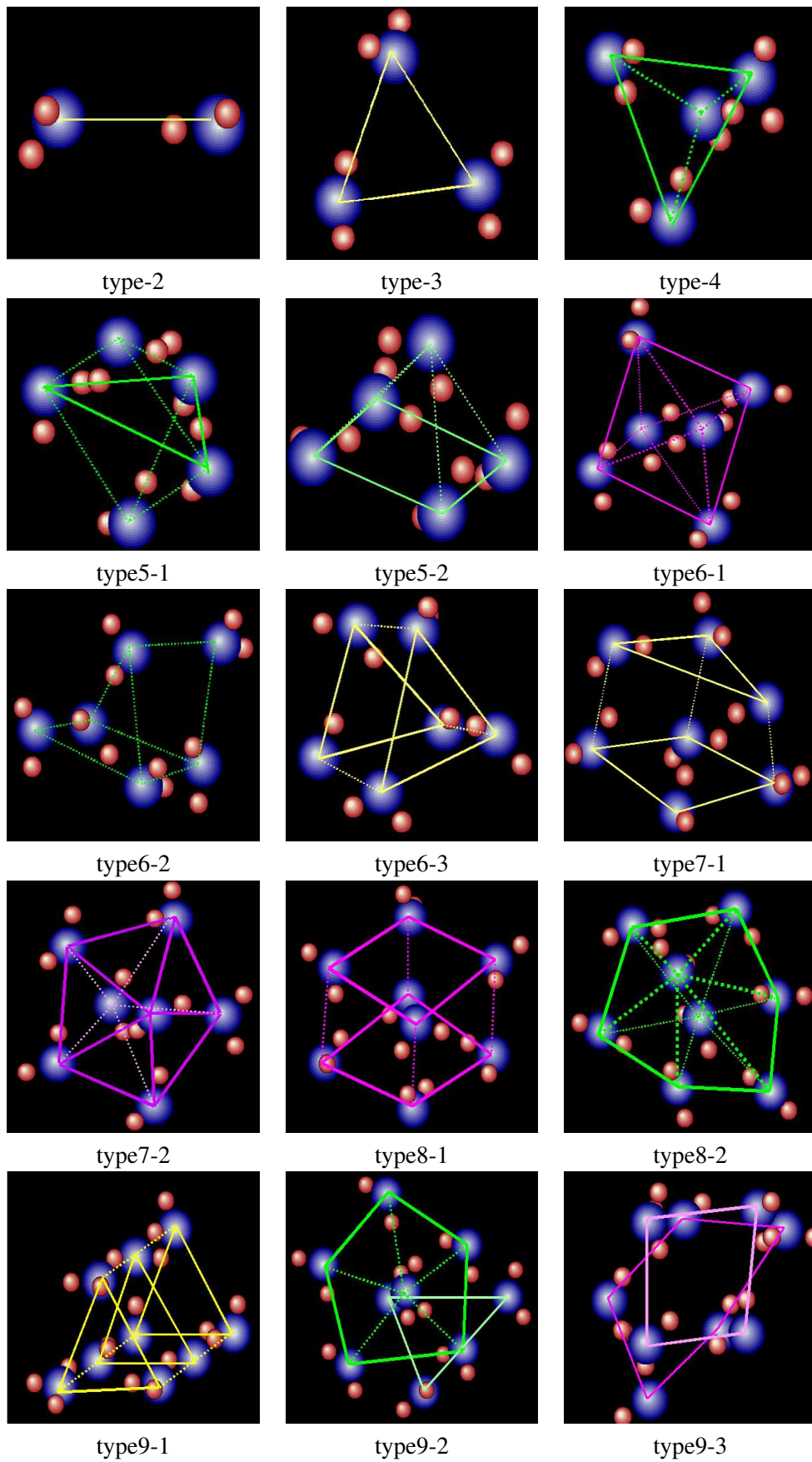


Fig. 1. The result of calculation

3.8 Simulation of gas aggregation cell by DSMC method

Y. Ito and I. Arai

We have developed a magnetron-sputter-type gas aggregation cluster source. This type of cluster source can generate clusters of high-melting point metal. In addition, the cluster source is smaller than our previously developed one. The apparatus is functionally divided into two parts, i.e., a magnetron sputtering part and a gas aggregation cell. In the magnetron sputtering part, ionized Ar atoms sputter the surface of the target mounted on the magnetron cathode producing a number of monomer atoms. The monomer atoms aggregate together into clusters in the gas aggregation cell, which is cooled by liquid nitrogen and is filled with carrier gas, i.e., a mixture of Ar and He. In the previous studies, it was found that the carrier gas could not flow smoothly in the aggregation cell. The reason was considered that the inlet position of carrier gas was located at the off-axial position. In deed, such asymmetry is thought to cause serious effect on the flow of carrier gas, resulting in strong suppression of cluster growth and yield. It is necessary to study further by taking account of real gas flow in the gas aggregation cell. To simulate the real gas flow as precisely as possible, we adopted a Direct Simulation Monte Carlo (DSMC) method[1]. Fig. 1(a) shows a result of DSMC calculation for the present configuration. In the figure, it is found that the velocity in x direction is negative around the target. This fact means that the carrier gas doesn't transport the monomer atoms around the magnetron in the present configuration as expected. Fig. 1(b) shows a result of DSMC calculation for the improved configuration, in which the inlet position is located at around the central axis. In the figure, the carrier gas flows smoothly from the inlet to the outlet, passing through the iris and the skimmer. These results of DSMC calculations suggest that the inlet position of carrier gas is very important for the proper operation of gas aggregation cluster source. The improved configuration is expected to enhance the cluster growth and yield.

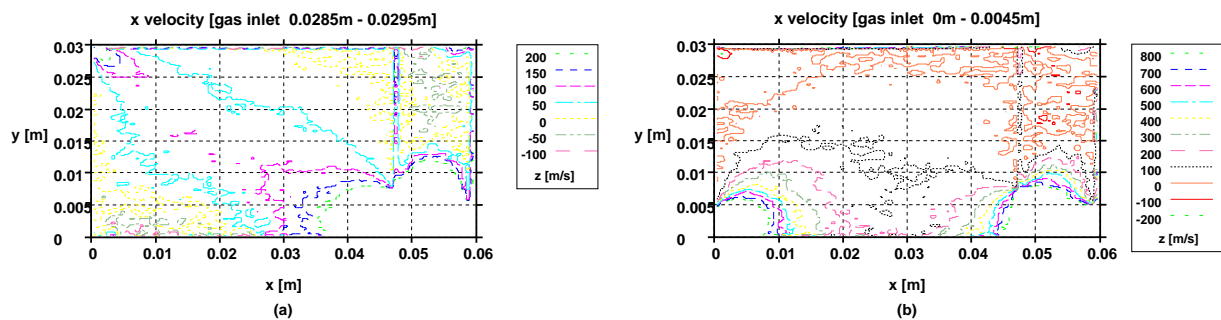


Fig. 1. Simulation of carrier gas (Ar) flow. The x direction is cell length and the y direction is cell radius. Magnetron cathode is $x=0\text{m}$, $y=0\text{m}\sim 0.0045\text{m}$. Iris is $x=0.048\text{m}$, $y=0\text{m}\sim 0.0075\text{m}$ and skimmer is $x=0.06$, $y=0\text{m}\sim 0.005\text{m}$. (a) Inlet position is $x=0\text{m}$, $y=0.0285\text{m}\sim 0.0295\text{m}$. (b) Inlet position is $x=0\text{m}$, $y=0\text{m}\sim 0.0045\text{m}$.

References

- [1] G. A. Bird, *Molecular Gas Dynamics and the Direct Simulation of Gas Flows*, (Oxford:Clarendon press)(1994)

4.

ACCELERATOR MASS SPECTROMETRY

4.1 Cosmogenic ^{36}Cl measurements in the Dome Fuji ice core, Antarctica

K. Sasa, Y. Matsushi³, Y. Tosaki, M. Tamari, T. Takahashi, M. Matsumura, K. Sueki, Y. Nagashima, H. Matsumura¹, N. Kinoshita¹, K. Bessho¹, K. Horiuchi², H. Matsuzaki³, Y. Shibata⁴, M. Hirabayashi⁵ and H. Motoyama⁵

We have measured cosmogenic nuclide ^{36}Cl in the ice core from the Dome Fuji station, Antarctica (39°42'12"E, 77°19'01"S, 3810 m a.s.l.) [1]. ^{36}Cl is a long-lived radionuclide with a half-life of 301 kyr. It is mainly produced in the stratosphere through spallation of ^{40}Ar by energetic primary and secondary cosmic rays. The global mean production rate of ^{36}Cl has been estimated to be ~ 20 atoms $\text{m}^{-2} \text{s}^{-1}$ [2].

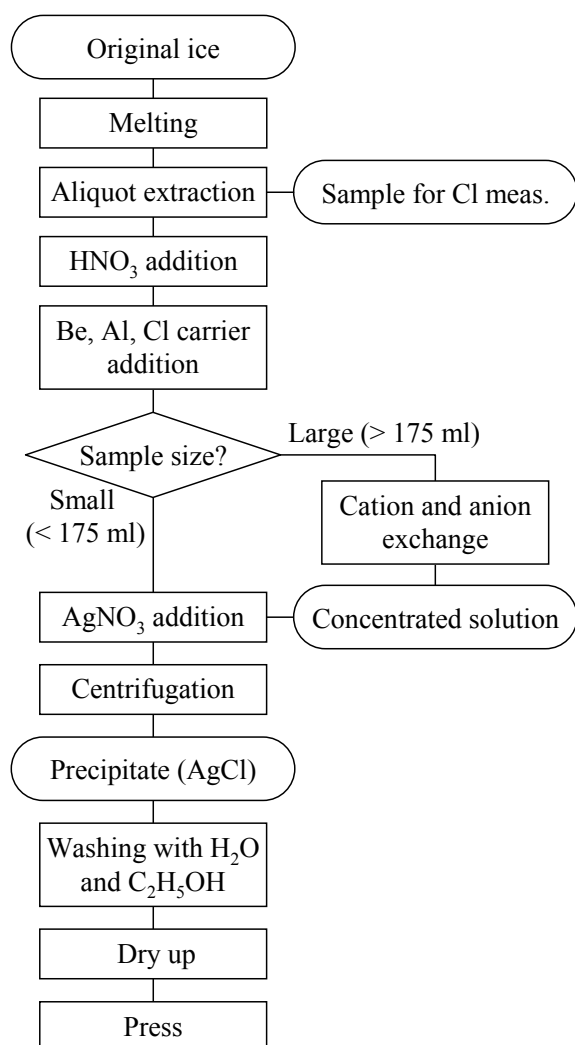


Fig. 1 Sample preparation scheme of ice samples for ^{36}Cl AMS.

The samples were mainly ice chips by-produced from the core trimmings for electrical conductivity measurements. The sample size was 0.1 to 1 kg, corresponding to the core length of 0.5 to 7 m per sample. The melted ice samples were spiked with 0.75–2 mg of Cl carrier, as $^{36}\text{Cl}/\text{Cl}$ ratio was to be 10^{-13} – 10^{-14} . Chloride ions in the sample were adsorbed on an anion exchange column and then eluted with HNO_3 . Finally, the sample was prepared as AgCl for AMS. Fig. 1 shows a sample preparation scheme of ice samples for ^{36}Cl AMS. The ^{36}Cl measurements were performed by accelerator mass spectrometry at the University of Tsukuba [3], for about 150 samples to date. The measurement precision was typically ± 7 – 8 %, estimated by the propagation of the reproductive error and the statistical error. Fig. 2 shows typical ^{36}Cl spectra for ^{36}Cl measurements of a standard sample (A), an ice sample (B) and a chemical blank (C). We usually used standard samples [4] of $^{36}\text{Cl}/\text{Cl} = 1.00 \times 10^{-11}$ and 1.60×10^{-12} for ice samples. The background with chemical blanks was better than 1×10^{-14} for the $^{36}\text{Cl}/\text{Cl}$ ratio.

The ^{36}Cl concentrations in the ice ranged from 2×10^4 atoms g^{-1} at the last glacial maximum to 1

¹ Radiation Science Center, High Energy Accelerator Research Organization

² Hirosaki University

³ Micro Analysis Laboratory, Tandem Accelerator, The University of Tokyo

⁴ National Institute for Environmental Studies

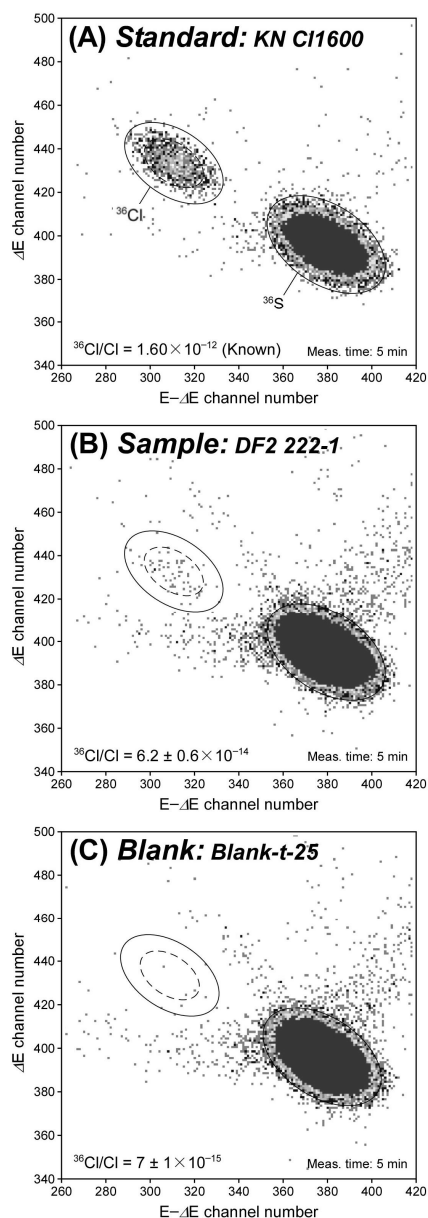


Fig. 2 ^{36}Cl spectra for ^{36}Cl measurements of a standard sample (A): $^{36}\text{Cl}/\text{Cl} = 1.60 \times 10^{-12}$, an ice sample (B) and a chemical blank (C).

Acknowledgements

This work is supported in part by the Grants-in-Aid for Scientific Research Program of the Ministry of Education, Culture, Sports, Science and Technology, Japan.

References

- [1] H. Motoyama, *Scientific Drilling* 5, (2007) 41–43.
- [2] D Huggle et al., *Planetary and Space Science* 44 (1996) 147–151.
- [3] K. Sasa et al., *Nucl. Instr. and Meth. B* 259 (2007) 41–46.
- [4] P. Sharma et al., *Nucl. Instr. and Meth. B* 52 (1990) 410–415.
- [5] K. Satow et al., *Polar Meteorol. Glaciol.*, 13 (1999) 43–52.

$\times 10^3$ atoms g^{-1} at the bottom of the core. The concentrations were converted to apparent ^{36}Cl flux onto the ice sheet, by using snow accumulation rate^[5] as a function of oxygen isotope ratio ($\delta^{18}\text{O}$). The apparent ^{36}Cl flux shows a clear decay profile throughout the core, being consistent with the model age-scale. The monotonic exponential decrease ensures the undisturbed stratigraphy of the core in spite of the increasing inclination of the ice layers below the depth of 2500 m. The ^{36}Cl flux seems to have been essentially constant at about $1\text{--}3 \times 10^4$ atoms $\text{cm}^{-2} \text{yr}^{-1}$ ($3\text{--}9$ atoms $\text{m}^{-2} \text{s}^{-1}$) for the past 720 kyr. This flux accords fairly with the value expected from latitudinal dependence of the nuclide fall-out.

The initial ^{36}Cl concentrations in the samples of $\delta^{18}\text{O} > -55\text{‰}$ showed slightly larger values than those expected from dilution during the interglacial periods. This implied the shift in the relationship between the moisture flux through the Antarctic air mass and isotopic composition of the vapor supplied onto the ice sheet during the glacial–interglacial transitions. The cosmogenic nuclide variations in the ice core have a potential for reconstructing various earth’s environments, not only the history of geomagnetic field intensity or solar activity, but especially paleo-conditions of polar atmospheric circulation.

⁵ National Institute of Polar Research

4.2 Residence times of spring waters on the foot of Mt. Fuji, estimated from bomb-produced ^{36}Cl

Y. Tosaki, N. Tase, K. Sasa, T. Takahashi and Y. Nagashima

Bomb-produced ^{36}Cl is a potential dating tool for modern groundwaters [1]. Although it has been utilized as an indicator of the presence of young water, studies focusing on its application as a dating tool are particularly infrequent [2]. Therefore, this study aims to provide a methodology on the estimation of groundwater residence time using bomb-produced ^{36}Cl . This is the first attempt to quantitatively utilize bomb-produced ^{36}Cl as a dating tool.

Water samples were collected in the Mt. Fuji area in August 2006 and March 2007. These samples include 28 spring water samples, and two groundwater samples from artesian flowing wells. Bicarbonate (HCO_3^-) concentrations were determined by titration with dilute H_2SO_4 solution. Other major ions (Na^+ , K^+ , Mg^{2+} , Ca^{2+} , Cl^- , SO_4^{2-} , NO_3^-) were measured by ion chromatography analysis (Ion Analyzer IA-100, Dkk-Toa). Dissolved SiO_2 concentrations were determined with an ICP-AES system (ICAP-757, Nippon Jarrell-Ash). Stable isotopic ratios ($\delta^{18}\text{O}$ and δD) were measured with a mass spectrometer (MAT252, Thermo Finnigan). The $^{36}\text{Cl}/\text{Cl}$ ratios of the samples were measured with the Tsukuba AMS system.

Figure 1A presents the spatial distribution of measured $^{36}\text{Cl}/\text{Cl}$ ratios. The $^{36}\text{Cl}/\text{Cl}$ ratios range from 4.3×10^{-14} to 4.12×10^{-13} . As shown in Figure 1A, investigated springs and groundwaters were classified into five regions (i.e. eastern, southeastern, southern and western fooths of Mt. Fuji, and foot of Mt. Ashitaka) using the altitude effect on $\delta^{18}\text{O}$ values. Relatively high $^{36}\text{Cl}/\text{Cl}$ ratios were found in the eastern part. Several spring waters from the southern foot exhibited high NO_3^- concentration, which were possibly under the influence of anthropogenic Cl. Therefore, the samples with high NO_3^- concentration (>10 mg/L) were excluded from further analyses.

In order to estimate residence times of these waters, time-series variation of $^{36}\text{Cl}/\text{Cl}$ in the Mt. Fuji area was estimated using the ^{36}Cl fallout data at the Dye-3 site, Greenland [3], and the total bomb-produced ^{36}Cl fallout obtained for the Tsukuba Upland (2.3×10^{12} atoms/ m^2) [4]. The ^{36}Cl flux for 1560–1920 AD at the Dye-3 site is 20 ± 6 atoms $\text{m}^{-2} \text{s}^{-1}$ [5], which can be taken as the natural background flux. This value was subtracted from annual values for 1945–1985 [3] to obtain yearly values of bomb-produced ^{36}Cl fallout at the Dye-3 site. These values were linearly scaled according to the assumed total fallout of 2.3×10^{12} atoms/ m^2 to predict the local fallout history of ^{36}Cl in the Mt. Fuji area.

To allow comparison with measured $^{36}\text{Cl}/\text{Cl}$ ratios of groundwater samples, the ^{36}Cl fallout values were converted to the $^{36}\text{Cl}/\text{Cl}$ unit using the following mass balance equation [6]:

$$R = \frac{F \times 3.156 \times 10^7}{P \times 10^{-3} \times C_p \times 6.022 \times 10^{23} / 35.45} \quad (1)$$

where R is the measured $^{36}\text{Cl}/\text{Cl}$ ratio, F is the ^{36}Cl fallout (atoms $\text{m}^{-2} \text{s}^{-1}$), P is the mean annual precipitation (mm), and C_p is the Cl^- concentration in the precipitation (mg/L).

Typical annual precipitation in the Mt. Fuji area, 2500 mm, e.g. [7], was used as P. The mean value

of four measured Cl^- concentrations at 780–2390 m in the investigated slopes (0.6 mg/L) [8] was used as C_p . The natural background $^{36}\text{Cl}/\text{Cl}$ ratio in the Mt. Fuji area was then added to the obtained R values. It was assumed to be 5×10^{-14} from the lower limit of measured $^{36}\text{Cl}/\text{Cl}$ ratios shown in Figure 2B. Figure 2A shows the estimated $^{36}\text{Cl}/\text{Cl}$ values obtained for the Mt. Fuji area.

As reported in previous studies, e.g. [9], most spring waters around Mt. Fuji originate from confined aquifers between lava layers or from the aquifer lying over the Older Fuji mud flow, which has low permeability. Piston flow would therefore be a reasonable approximation in this area. Based on this assumption, residence times of spring waters can be estimated by comparing Figure 2A and Figure 2B. Considering the earlier results in 1960s [10], which showed elevated levels of tritium, most of the spring waters would have been recharged in the post-bomb period. Hence, estimated residence times were basically obtained using the post-peak part of the curve shown in Figure 2A.

Figure 1B shows the distribution of estimated residence times for spring waters and groundwaters. Residence times of less than 20 yr for the southeastern foot are consistent with previous estimates of ~10 yr by the $^3\text{H}/^3\text{He}$ dating method [11]. Residence times of 25–35 yr estimated for the eastern foot are also in agreement with the fact that higher ^3H concentrations (~38 TU) were measured in the eastern foot than those of the southeastern foot in 1983 [12]. While, residence times of 25–30 yr obtained for the western foot disagree with a high ^3H concentration measured in 1969 [13], which indicated bomb-derived ^3H .

Four samples from the western foot have $^{36}\text{Cl}/\text{Cl}$ ratios of $\sim 1 \times 10^{-13}$ (Figure 1A), which is more than twice of the assumed natural background (5×10^{-14}). One reasonable explanation for the disagreement in residence times may be that the natural background level of $^{36}\text{Cl}/\text{Cl}$ for the western foot is higher than that for other foots under investigation. This can be caused by the difference in the Cl^- concentration in precipitation; lesser stable chloride supply leads to the higher $^{36}\text{Cl}/\text{Cl}$ ratio.

Condition of the recharge area (i.e. the natural background $^{36}\text{Cl}/\text{Cl}$ ratio, chloride concentration in precipitation, and mean annual precipitation) has to be known correctly, otherwise errors may be directly enlarged in estimating residence times. However the results obtained show the fundamental reasonability of the method using bomb-produced ^{36}Cl to estimate groundwater residence time.

References

- [1] H.W. Bentley, F.M. Phillips, S.N. Davis, S. Gifford, D. Elmore, L.E. Tubbs, H.E. Gove, *Nature* 300 (1982) 737.
- [2] Y. Tosaki, N. Tase, G. Massmann, Y. Nagashima, R. Seki, T. Takahashi, K. Sasa, K. Sueki, T. Matsuhiro, T. Miura, K. Bessho, H. Matsumura, M. He, *Nucl. Instr. and Meth. B* 259 (2007) 479.
- [3] H.-A. Synal, J. Beer, G. Bonani, M. Suter, W. Wölfli, *Nucl. Instr. and Meth. B* 52 (1990) 483.
- [4] Y. Tosaki, N. Tase, M. Yasuhara, Y. Nagashima, K. Sasa, T. Takahashi, *Hydrol. Res. Lett.* 2 (2008) 9.
- [5] H.-A. Synal, J. Beer, G. Bonani, Ch. Lukasczyk, M. Suter, *Nucl. Instr. and Meth. B* 92 (1994) 79.
- [6] J.N. Andrews, W.M. Edmunds, P.L. Smedley, J.-Ch. Fontes, L.K. Fifield, G.L. Allan, *Earth Planet. Sci. Lett.* 122 (1994) 159.
- [7] S. Yamamoto, *Geogr. Rev. Japan* 43 (1970) 267 (in Japanese with English abstract).
- [8] T. Hiyama, A. Sato, M. Yasuhara, A. Marui, Y. Suzuki, S. Takayama, *Bull. Environ. Res. Cent. Univ.*

Tsukuba 20 (1995) 45 (in Japanese with English title).

- [9] R. Tsuchi, in: Aramaki, S., Fujii, T., Nakada, S. and Miyaji, N. (Eds.), *Fuji Volcano*, Yamanashi Institute of Environmental Sciences, Fujiyoshida, 2007, p. 375 (in Japanese with English abstract).
- [10] T. Ochiai, H. Kawasaki, *Bull. Agric. Eng. Res. Stn.* 8 (1970) 67 (in Japanese with English summary).
- [11] Y. Mahara, T. Igarashi, Y. Tanaka, *J. Groundwater Hydrol.* 35 (1993) 201 (in Japanese with English abstract).
- [12] R. Yoshioka, K. Kitaoka, N. Koizumi, *J. Groundwater Hydrol.* 35 (1993) 271 (in Japanese with English abstract).
- [13] H. Kawasaki, *J. Jap. Assoc. Groundwater Hydrol.* 20 (1978) 117 (in Japanese with English abstract).

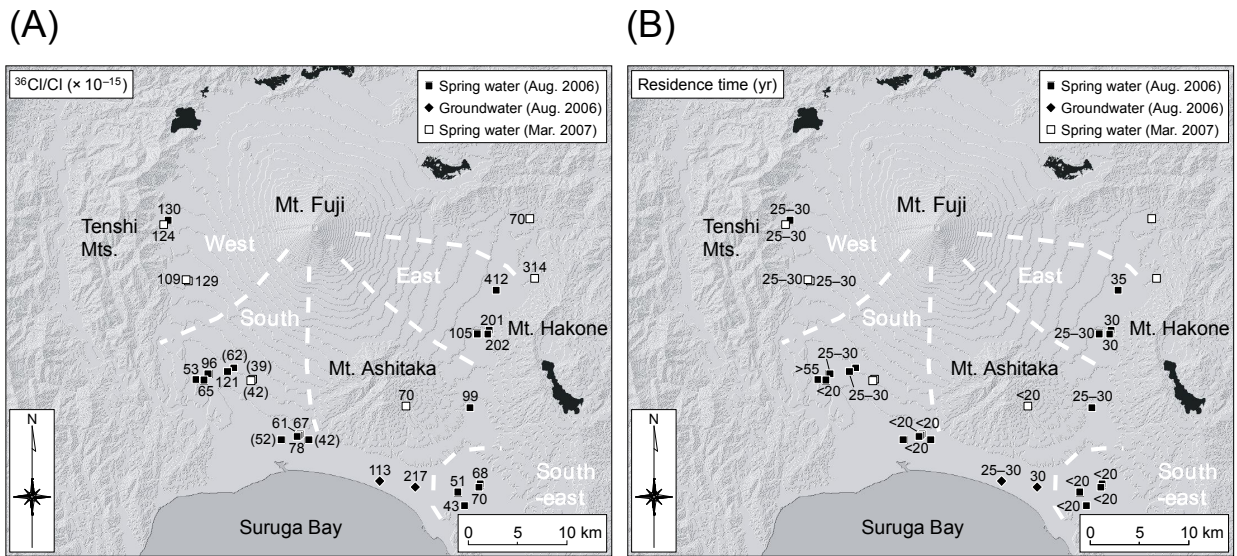


Figure 1. (A) Spatial distribution of $^{36}\text{Cl}/\text{Cl}$ ratios in spring waters and groundwaters in the Mt. Fuji area. Values in parentheses represent the samples with high NO_3^- concentration (>10 mg/L). (B) Spatial distribution of residence times of spring waters and groundwaters, estimated from ^{36}Cl .

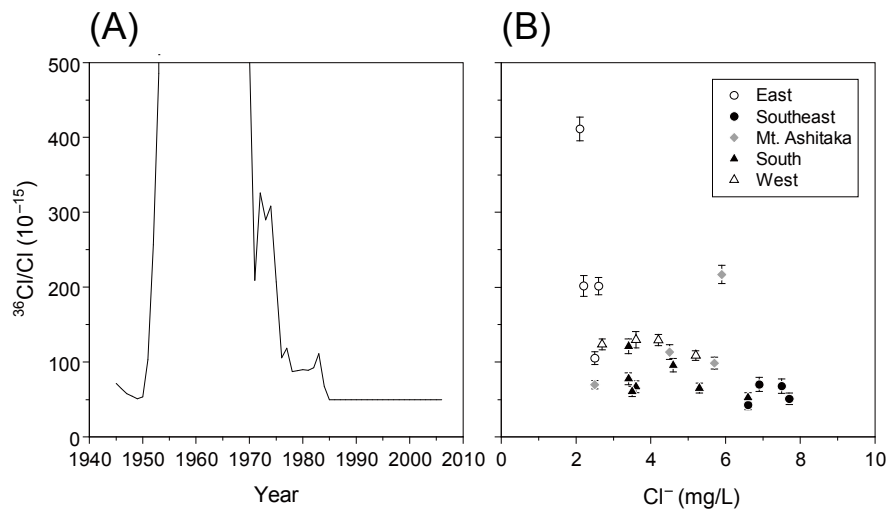


Figure 2. (A) Estimated time-series variation of $^{36}\text{Cl}/\text{Cl}$ in the Mt. Fuji area. (B) Measured $^{36}\text{Cl}/\text{Cl}$ ratios in spring waters and groundwaters, plotted against chloride concentration.

4.3 Measurement of in situ-produced cosmogenic ^{36}Cl in calcite

Y. Matsushi¹, K. Sasa, T. Takahashi, Y. Nagashima and Y. Matsukura

Introduction

Cosmogenic ^{36}Cl in calcite is produced in-situ via ^{40}Ca spallation, muon capture by ^{40}Ca , and absorption of spallation or muon-induced thermal neutron by ^{35}Cl [1]. The nuclide is a geomorphological tool for quantifying exposure age or denudation rate of limestone surfaces. A correct estimation of the age or rate requires accurate measurement of ^{36}Cl and appropriate scaling of ^{36}Cl production rate, which depend on Cl concentration in the limestone samples. However, the samples are usually dissolved with nitric acid; therefore it becomes difficult to measure Cl concentration because of the abundant nitric ions in the solution. Ion-selective electrode method is an available alternative, but it is often elaborate and time-consuming for the low pH and low Cl concentration samples. Here we apply isotope dilution method using a ^{35}Cl -enriched carrier [2]. This methodology enables us to measure Cl content in the samples concurrently with ^{36}Cl -AMS (Accelerator Mass Spectrometry), without any complicated procedure.

Materials and method

Limestone samples for the test analysis were collected from the topmost 5 cm of an exposed pinnacle at Akiyoshi and Hirao karst areas, Japan (Table 1). The rock samples were crushed and sieved to 0.5–0.125 mm size. Twice of HNO_3 leaching eliminated the meteoric ^{36}Cl and other potential contamination, resulting in ~10% dissolution of the particle surfaces. The leached samples (~10 g) were soaked with ~50 ml of ultrapure water, and dissolved gradually with ~50 ml of 4 mol/L HNO_3 .

A Na^{35}Cl powder from Aldrich Co. (^{35}Cl purity: 99 atom%) was used as a carrier. Each samples and chemical blanks were spiked with 1.5 mg of ^{35}Cl . Blank A was also spiked with 0.5 mg of normal Cl carrier, as a test standard of the known content of initial Cl with the natural isotope ratio (Table 1). Cl^- in the samples were recovered as AgCl precipitate and pressed into the cathode cones.

^{36}Cl -AMS was performed with the Tsukuba AMS-system [3], by using an AMS-standard with the known $^{36}\text{Cl}/\text{Cl}$ ratio of 1.60×10^{-12} [4]. $^{35}\text{Cl}/^{37}\text{Cl}$ ratio was monitored with Faraday cups at the AMS-ion source. A data-logging system recorded automatically the integrated current of the ^{35}Cl and ^{37}Cl ion-beams, and ^{36}Cl counts at the final detector, for the every ~3–5 min measurement of the target samples.

Table 1. Samples, carrier spiked, and results of the measurement

Sample ID	Net rock wt. (g)	Carrier wt. (mg Cl)		$^{35}\text{Cl}/^{37}\text{Cl}$	$^{36}\text{Cl}/^{35}\text{Cl}$ (10^{-13})	Initial Cl content (ppm)	^{36}Cl activity (10^5 atom g^{-1})
		Normal	Enriched				
Blank A	–	0.505	1.537	14.6±0.03	–	0.530±0.003*	–
Blank B	–	–	1.516	286±11	0.07±0.02	–	–
Akiyoshi	9.6688	–	1.512	24.3±0.1	3.43±0.23	28.1±0.2	10.4±0.7
Hirao	8.9602	–	1.516	21±2	–	37±5	–

* Weight in mg of the normal Cl carrier calculated from $^{35}\text{Cl}/^{37}\text{Cl}$ data.

¹ MALT (Micro Analysis Laboratory, Tandem accelerator), The Univ. of Tokyo (E-mail: matsushi@n.t.u-tokyo.ac.jp).

Results and discussion

Figure 1 shows the monitored $^{35}\text{Cl}/^{37}\text{Cl}$ ratio, with the data from ordinary ‘normal’ samples including AMS-standards, chemical blanks, and natural samples measured during the latter half of the 2007 period. The isotope ratio of the ‘normal’ samples exhibited the fairly constant values of 3.16 ± 0.05 , which consistent with the natural $^{35}\text{Cl}/^{37}\text{Cl}$ ratio (3.127). The ‘spiked’ samples show distinctly large $^{35}\text{Cl}/^{37}\text{Cl}$ ratios, ranging from 286 ± 11 (Blank B) to 14.60 ± 0.03 (Blank A). The ratio of 286 ± 11 means the ^{35}Cl purity of 99.65 ± 0.01 atom% in the spiked carrier, as is expected from [2].

The $^{36}\text{Cl}/^{35}\text{Cl}$ ratio of the Akiyoshi sample was $(3.43\pm 0.23) \times 10^{-13}$ (Table 1); the background of $(7\pm 2) \times 10^{-15}$ (Blank B) had been subtracted. Unfortunately, the $^{36}\text{Cl}/^{35}\text{Cl}$ ratio of the Hirao sample was not able to be measured, because of the severe sulfur contamination.

The natural (or initial) content of Cl in a ^{35}Cl -spiked sample is calculated to as:

$$[\text{Cl}_{\text{nat.}}] = [\text{Cl}_{\text{spike}}] \cdot \frac{S - M}{M - N} \cdot \frac{1 + N}{1 + S} \quad (1)$$

where, $[\text{Cl}_{\text{nat.}}]$ and $[\text{Cl}_{\text{spike}}]$ are natural and spiked total $^{(35+37)}\text{Cl}$ (atom), N, S, and M are natural, spiked, and measured $^{35}\text{Cl}/^{37}\text{Cl}$ ratios, respectively. Here, the ^{36}Cl activity is then calculated to as:

$$[^{36}\text{Cl}] = [\text{Cl}_{\text{spike}}] \cdot \frac{S - N}{M - N} \cdot \frac{M}{1 + S} \cdot R_{\text{AMS}} \quad (2)$$

where, $[^{36}\text{Cl}]$ is the ^{36}Cl amount in the sample (atom), R_{AMS} is the $^{36}\text{Cl}/^{35}\text{Cl}$ ratio obtained by AMS.

Calculation from Eq. (1) overestimates the initial Cl content in the Blank A by $\sim 5\%$ (Table 1). The reason for this slight discrepancy is not clear at present. The natural Cl content in the Akiyoshi and Hirao limestones were calculated to be 28.1 ± 0.2 and 37 ± 5 ppm, respectively (Table 1). From Eq. (2), the ^{36}Cl concentration in the Akiyoshi limestone was calculated to be $(10.4\pm 0.7) \times 10^5$ atom g^{-1} (Table 1).

The data in this study provide the initial results of the cosmogenic ^{36}Cl measurement in calcite in Japan. The isotope dilution method works very well at UTTAC, with a sufficient accuracy for the Cl and ^{36}Cl quantification. Now we are moving toward a routine application of this methodology for the systematic ^{36}Cl measurement that targets several Japanese karsts under subtropical to subarctic environments.

References

- [1] J.O.H. Stone et al., *Geochim. Cosmochim. Acta* **62** (1998) 433.
- [2] D. Desilets et al., *Chem. Geol.* **233** (2006) 185.
- [3] K. Sasa et al., *Nucl. Instr. and Meth.* **B259** (2007) 41.
- [4] P. Sharma et al., *Nucl. Instr. and Meth.* **B52** (1990) 410.

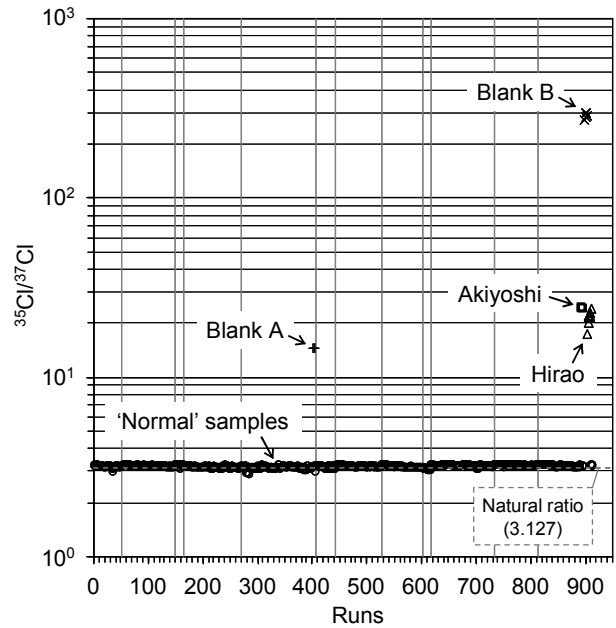


Fig.1. $^{35}\text{Cl}/^{37}\text{Cl}$ ratios. Vertical lines indicate hiatus between the measurements.

4.4 Depth profile of $^{36}\text{Cl}/^{35}\text{Cl}$ induced in the thick concrete shield in EP-1 beam line at the 12-GeV proton synchrotron facility, KEK

N. Kinoshita¹, H. Matsumura¹, K. Bessho¹, Y. Matsushi², K. Sasa³, T. Takahashi³, S. Mihara³, T. Oki³, M. Matsumura³, Y. Tosaki³, K. Sueki³, M. Tamari³ and Y. Nagashima³

Secondary particles are produced by bombarding target and beam dump etc. with primary beam in an accelerator facilities. The secondary particles activate the shielding walls and the various materials around accelerator. We have measured depth profiles of several radioisotopes in shielding concrete at various facilities using a gamma-ray spectrometry. Cl-36, produced in a shielding wall by a thermal neutron capture and nuclear spallation reaction, is one of candidates to measure an aspect of activation in the shielding wall with an accelerator mass spectrometry.

The method for preparing Cl-36 AMS targets was described in the previous report [1]. Chloride ion was extracted from 1 – 20 g of the concretes to 15 – 50 ml of 10 mM nitric acid in a Teflon pressurized decomposition vessel at 130 °C for 12 hours. The concentration of chlorine in the solution was determined by ion chromatography. The $^{36}\text{Cl}/^{nat}\text{Cl}$ atomic ratio in the solution was isotopically diluted with a known amount of NaCl standard solutions (with a natural isotopic abundance). Trace amount of S^{2-} occurring in the solution was oxidized to SO_4^{2-} by adding a H_2O_2 solution, then Cl ion was recovered as AgCl precipitate by adding AgNO_3 solution. After dissolving the AgCl precipitate in an aqueous ammonium solution, $\text{Ba}(\text{NO}_3)_2$ solution was added to remove sulfur as BaSO_4 precipitate. The Cl ion was re-converted to AgCl precipitate by acidifying with HNO_3 . It was washed with water, dried and subjected to Cl-36 AMS at UTTAC, University of Tsukuba [2].

The three dimensional spectrum by an ionization chamber was shown in Fig. 1 as an example.

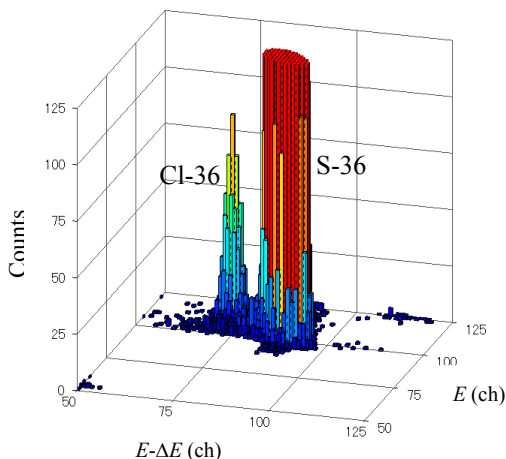


Fig. 1. Three dimensional spectrum of 150 cm. $^{36}\text{Cl}/^{35}\text{Cl}$ atomic ratio was measured to be 2.2×10^{-12} .

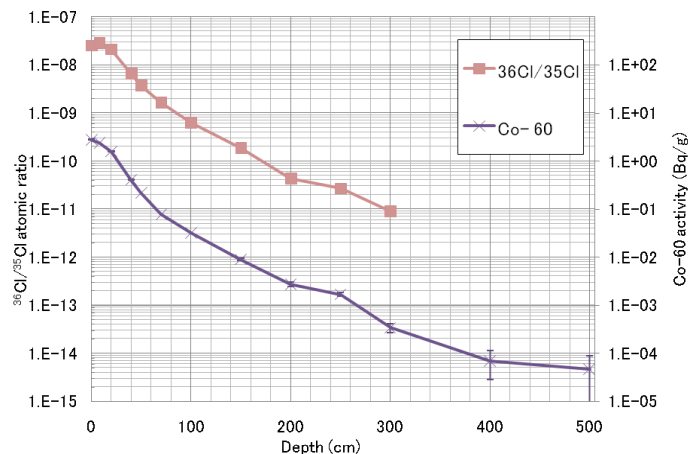


Fig. 2. Depth profile of $^{36}\text{Cl}/^{35}\text{Cl}$ atomic ratio (left scale) and Co-60 activity (right scale).

¹ Radiation Science Center, High Energy Accelerator Research Organization, 305-0801 Ibaraki, Japan.

² Micro Analysis Laboratory, Tandem Accelerator, University of Tokyo, 113-0032 Tokyo, Japan.

³ Research Facility Center, University of Tsukuba, 305-8577 Ibaraki, Japan.

We succeeded in discriminating Cl-36 event from isobar S-36. Depth profile of Cl-36 in the shielding concrete was shown in Fig. 2 together with a gamma emitting nuclide Co-60, produced by neutron capture reaction, which was determined with a HPGe detector. Cl-36 could be produced by both a thermal neutron capture reaction and a nuclear spallation reaction. We could estimate the ratio produced from a thermal neutron capture and a nuclear spallation reaction. Thermal neutron flux could be estimated from the depth profiles of Co-60 using a generally reported thermal neutron capture cross section. Radioactivities derived from the flux and cross sections of $^{35}\text{Cl}(n,\gamma)^{36}\text{Cl}$ by a thermal neutron show the contribution from the thermal neutron capture reaction. Radioactivity, which the contribution from the thermal neutron capture was subtracted from the measured activity, shows the contribution from the nuclear spallation reaction. Production ratios were estimated to be approximately 30% from the neutron capture and 70% from the spallation.

References

- [1] K. Bessho, H. Matsumura, T. Miura, Q. B. Wang, K. Masumoto, T. Tatsuhiro, Y. Nagashima, R. Seki, T. Takahashi, K. Sasa and K. Sueki, *Radiochim. Acta*, 94, 801 (2006).
- [2] K. Sasa, Y. Nagashima, T. Takahashi, R. Seki, Y. Tosaki, K. Sueki, K. Bessho, H. matsumura, T. Miura and M. He, *Nucl. Instr. Meth. B*, 259, 41 (2007).

4.5 Chlorine-36 in Gibeon iron meteorite

Y. Oura¹, F. Hashizume¹, M. Ebihara¹, Y. Tosaki, K. Sasa, Y. Nagashima, T. Takahashi, M. Tamari, K. Sueki, S. Mihara, T. Oki, Y. Matsushi², H. Matsumura³, K. Bessho³, N. Kinoshita³, T. Miura³

Gibeon iron meteorite was found in 1836 in the present Republic of Namibia. Many fragments were found at the area longer than 400 km and their total weight is estimated to be about 21 tons, a one of the popular large meteorite. Contents of noble gas stable isotopes, ¹⁰Be, and ²⁶Al produced by spallation reaction by cosmic ray have been analyzed in a lot of specimens. ⁵³Mn and ³⁶Cl concentrations were also obtained. Then it was found that Gibeon fragments were classified into two groups by their cosmic ray exposure age calculated by ¹⁰Be/²¹Ne method. The reason that Gibeon has two exposure ages is still unclear. We have been determining ⁵³Mn and ³⁶Cl in Gibeon iron meteorite by neutron activation analysis and AMS method, respectively, to clarify an exposure history of Gibeon meteorite. And a development of NAA technique to determine trace contents of ⁵³Mn in a deep specimen is also our objective. Since there is no standard reference material for cosmogenic nuclides to evaluate observed content values, it is important to determine two nuclides for comparison of their content values each other. ³⁶Cl contents can give alternative ages based on ³⁶Cl/³⁶Ar method.

Nine samples including a fragment called Railway-A were analyzed. After dissolution of a sample with Cl and Mn carriers in HNO₃, Cl and Mn fractions were separated chemically. For AMS, AgCl precipitates were prepared and ³⁶Cl/Cl ratios were determined by AMS at the Tandem Accelerator Complex, University of Tsukuba. The determination of ⁵³Mn was not performed yet.

Eight samples other than Railway-A belong to Group-2, whose exposure ages are younger than Group-1, and their ¹⁰Be contents were already obtained. In Fig.1 the correlation between ³⁶Cl and ¹⁰Be contents is shown. In this study the similar correlation was observed for Group-2. The variation for Group-2 is larger than for Group-1.

Nord and Zaehring [1] reported noble gas isotope contents in Railway of Gibeon. In their report, however, there is an inconsistent between an exposure age and noble gas contents. Thus we analyzed Railway to examine it. Noble gas contents were determined by Prof. Nagao, University of Tokyo. Consequently exposure ages of 1×10^7 years and 4×10^7 years were obtained by ¹⁰Be/²¹Ne and ³⁶Ar/³⁶Cl methods, respectively. So it was evident that Railway was categorized by Group-2.

References

[1] R. Nord and J. Zaehring, *Geochimii I Analiticeskoy Chimii, Akad. Nauk* 59 (1972).

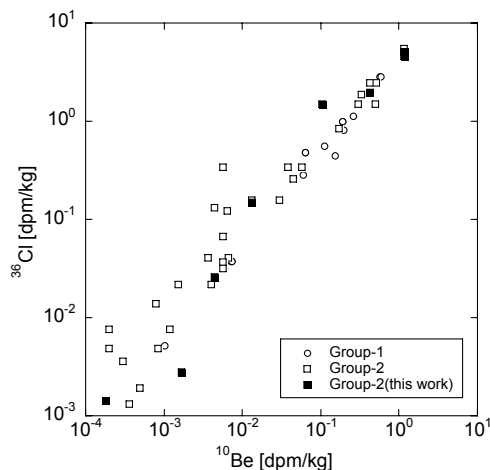


Fig.1 Correlation between ¹⁰Be and ³⁶Cl in Gibeon.

¹ Graduate School of Science and Engineering, Tokyo Metropolitan University

² Micro Analysis Laboratory, Tandem Accelerator, University of Tokyo

³ Radiation Science Center, High Energy Accelerator Research Organization

5.

INTERDISCIPLINARY RESEARCH

5.1 Development of radiation environment monitors for use in spacecraft

Y. Sasaki¹, H. Matsumoto¹, K. Sasa, Y. Tagishi, Y. Nagashima

The space radiation environment is of primary concern for space engineering because it can damage electronic devices and structural material on spacecraft, thereby limiting their lifetime. To investigate radiation effects on spacecraft, we used on-board monitors to observe the orbital radiation environment [1]. Accumulated data related to the space radiation environment are expected to facilitate the development of reliable spacecraft and contribute greatly to the success of space missions. In fiscal 2007, we manufactured a new radiation environment monitor system as a component of the Greenhouse gases Observing Satellite. We calibrated its telescopes using a proton beam from the University of Tsukuba's 12UD pelletron accelerator.

Figure 1 and Table 1 show the telescopes under beam testing with their performance specifications. Figure 2 shows a schematic layout of this testing with a cross-sectional view. As Fig. 2 shows, the telescopes comprise stacked silicon detectors with a Tantrum collimator. A primary mono-energy beam was irradiated to a 1- μm -thick Au foil target. A secondary beam scattered at the Au foil was incident on the silicon detectors in the telescopes, having roughly equal energy to that of the primary beam. The beam energy was adjusted from 4 MeV to 16 MeV in steps.

Through testing, we determined the energy response and energy resolution of the silicon detectors. As an example, Fig. 3 portrays the energy responses of the silicon detectors installed in the APS-B telescope as a function of the energy deposited.



Fig. 1. Exterior view of the telescopes

Table 1. Performance specifications of the telescopes under the beam testing

Parameter	Telescope	
	APS-A	APS-B
Quantity	5	2
Geometric factor ($\text{cm}^2 \text{sr}$)	0.04	0.06
Field of view (full angle) (deg)	44	44
Mass (kg)	1.3	1.3
Dimension (mm)	120×90×65	120×90×86
Power (W)	1.1	1.1

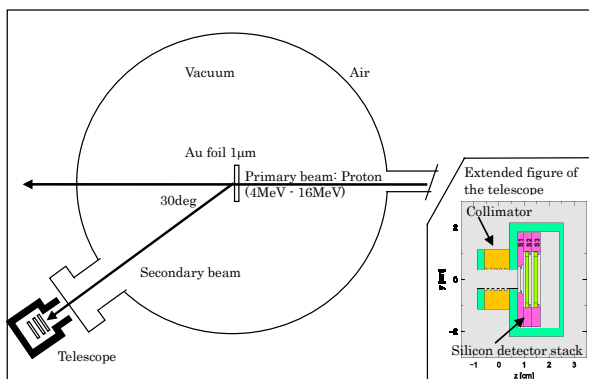


Fig. 2. Schematic layout of the beam testing

¹ Japan Aerospace Exploration Agency

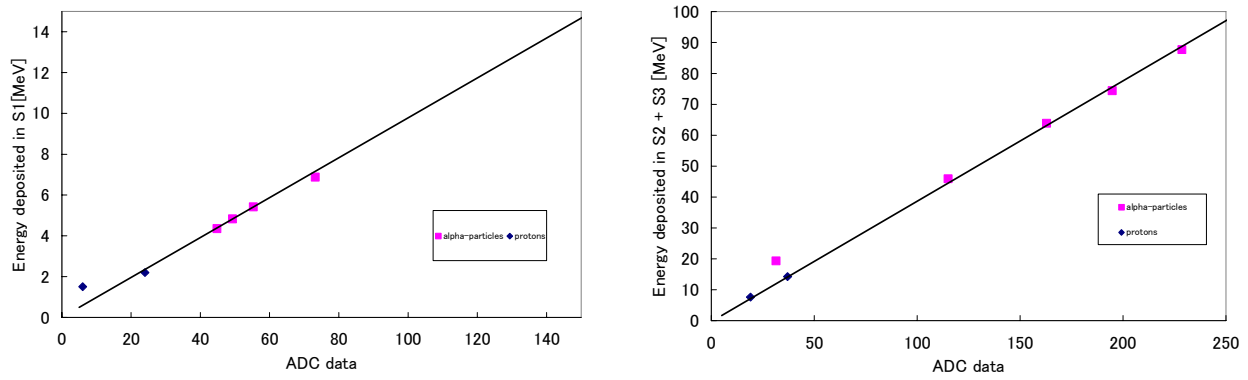


Fig. 3. Energy responses of APS-B silicon detectors to mono-energy protons incorporated into the responses to alpha-particles resulted from the other experiment

References

- [1] T. Goka, H. Matsumoto, Measurement of Near Earth Radiation Environment – Overview and Plan –, IAC-06-D5.2.02, 57th IAC, Valencia, 2006.

5.2 Micro-PIXE analysis of rare-earth elements in monazite

M. Kurosawa, S. Ishii and K. Sasa

Introduction

Monazite, $(\text{Ce, La, Nd, Th})\text{PO}_4$, is an important mineral for resource of rare-earth elements (REE), U-Th-Pb age determination in geological sciences [1], and natural background radiation in coastal area [2]. Thus, accurate and precise determinations of the chemical compositions are important for the geological and environmental researches. In the analyses, determinations of all of the REE concentrations are desirable because relative ratios among the most REE contents are an important indicator for crystal fractionation, melting, and crystallization sequence in magmatic processes. The determinations of the all REE contents in the crustal materials are required for evaluation of REE resources. Chemical analyses of monazite are often performed by electron microprobe (EPMA) because of the convenience and the reliability. Contents of REE oxide in common monazite are a few to 30 wt% for light REE (La to Eu) and several tens to hundreds wt. ppm for heavy REE (Gd to Lu), respectively. Lower quantification limits of EPMA are about several thousand wt. ppm, so the determinations of the heavy REE are difficult.

For these reasons, we attempted to determine precisely REE contents in monazite by using particle-induced X-ray emission (PIXE) which is possible to determine most of elements with concentration of a few wt ppm in solid materials. PIXE analyses are based on energy-dispersive spectrometry of characteristic X-rays emitted from sample material, so overlaps of several X-ray peaks in the measured spectrum sometimes occur because of inadequate energy resolution of the X-ray detector. Thus, a subtraction calculation of X-ray intensities of overlapped peaks from an interest X-ray intensity is necessary for determinations of the interest elemental concentration. The subtraction requires the accurate relative line intensities of K and L X-ray peaks and calculations of the relative line intensities modified by X-ray absorption due to sample matrix. In this study, the subtraction calculations using the reasonable relative line intensities were reexamined and REE contents in monazite were determined using the new calculation method.

Subtraction of overlapped X-ray peaks and quantification

Most rare-earth element minerals contain P, Si, Ca, Sc, Ti, Mn, Fe, Y, Zr, Nb, Sn, REE, Hf, Ta, W, Pb, Th, and U, so several peaks of K and L-X rays of their elements are overlapped in the PIXE spectra. The overlapping peaks are showing in Table 1. The overlapped intensities are subtracted based on X-ray intensities of K_α and L_α peaks of interest elements and the relative line intensities of K_β , $L_{\beta 1}$, $L_{\beta 2}$, $L_{\beta 3}$, $L_{\beta 4}$, $L_{\beta 6}$, $L_{\gamma 1}$, $L_{\gamma 2}$, $L_{\gamma 3}$, and L_I for the K_α and L_α peaks. In this study, data from Scofield [3] and Campbell et al [4] were used for the relative line intensities of K X-rays and data combined Cohen and Harrigan [5] and Reis and Jesus [6] were used for the relative line intensities of L X-rays. Relative line intensities of most elements calculated based on these data and X-ray absorption due to sample matrix agreed well with the relative line intensities observed at the PIXE measurement of several standard materials.

Quantification for elements in monazite was performed by using the model calculation of

Table 1. Overlapped X-ray peaks at PIXE measurements of rare-element minerals.

X-ray peak (keV)*	Overlapped X-ray peak (keV)	Overlapped X-ray peak (keV)
P K _α 2.010	Y L _{β2} (2.078)	Y L _{β3} (2.072)
Sc K _α 4.091	Ca K _β (4.013)	
Ti K _α 4.511	Sc K _β (4.461)	
Mn K _α 5.898	Nd L _{β3} (5.823)	Ho L ₁ (5.943)
Fe K _α 6.403	Ce L _{γ2} (6.326)	Ce L _{γ3} (6.342)
Y K _α 14.958	Pb L _{γ2} (15.097)	
Zr K _α 15.775	Th L _{β2} (15.605)	U L _{β6} (15.727)
Nb K _α 16.615	Y K _β (16.738)	U L _{β4} (16.577)
Ce L _{α1} 4.840	Ti K _β (4.932)	
Pr L _{α1} 5.033	La L _{β1} (5.042)	La L _{β3} (5.143)
Nd L _{α1} 5.230	Ce L _{β1} (5.263)	La L _{β3} (5.143)
Sm L _{α1} 5.636	Ce L _{β2} (5.613)	Nd L _{β1} (5.722)
Gd L _{α1} 6.058	Ce L _{γ1} (6.054)	La L _{γ2} (6.060)
	La L _{γ3} (6.075)	Nd L _{β2} (6.090)
Tb L _{α1} 6.273	Sm L _{β1} (6.206)	Sm L _{β3} (6.317)
Dy L _{α1} 6.495	Fe K _α (6.403)	Mn K _β (6.493)
	Sm L _{β2} (6.587)	Nd L _{γ1} (6.604)
Ho L _{α1} 6.720	Gd L _{β1} (6.713)	Lu L ₁ (6.753)
	Gd L _{β3} (6.832)	
Er L _{α1} 6.949	Tb L _{β1} (6.977)	Fe K _β (7.060)
	Tb L _{β3} (7.097)	Gd L _{β2} (7.102)
	Nd L _{γ2} (6.883)	Nd L _{γ3} (6.901)
Tm L _{α1} 7.180	Sm L _{γ1} (7.183)	Ta L ₁ (7.173)
	Dy L _{β1} (7.248)	
Yb L _{α1} 7.416	Tb L _{β2} (7.367)	Dy L _{β3} (7.370)
	Sm L _{γ2} (7.471)	Sm L _{γ3} (7.489)
	Ho L _{β1} (7.526)	
Lu L _{α1} 7.656	Dy L _{β2} (7.636)	Ho L _{β3} (7.653)
	Gd L _{γ1} (7.790)	Er L _{β1} (7.811)
Ta L _{α1} 8.146	Tm L _{β1} (8.102)	Gd L _{γ3} (8.105)
	Tb L _{γ1} (8.105)	Er L _{β2} (8.186)
	Tm L _{β3} (8.231)	
W L _{α1} 8.398	Tb L _{γ2} (8.398)	Yb L _{β1} (8.402)
	Tb L _{γ3} (8.423)	Dy L _{γ1} (8.426)
	Tm L _{β2} (8.468)	
Pb L _{α1} 10.551	Hf L _{γ1} (10.516)	Lu L _{γ2} (10.460)
	Lu L _{γ3} (10.511)	

*X-ray energy (Table of Isotope, 8th Ed.)

Sample and instrumentation

A monazite used in this study was collected from a pegmatite dyke in a Cretaceous Abukuma granite body at Ishikawa town, Fukushima Prefecture, northeast Japan. The monazite was an elongated euhedral crystal, 3 mm wide x 10 mm length, with yellowish pale brown, and was occurred from a grain boundary of giant microcline in the intermediate zone of the pegmatite. A slightly chemical zoning was observed with optical microscope. The sample was cut and double-polished, and then mounted on the slide glass. The sample surface was coated by a carbon film to avoid electrostatic charging.

The PIXE analyses were performed at the 1MV Tandetron. A 0.1 nA beam of 1.92-MeV proton was focused to a 24 x 24 mm spot on the sample using slits and magnetic lenses. The beam incidence was normal to the sample surface, and the X-ray measurement take-off angle was 45° [9]. The characteristic

Campbell [7]. Intensities of X-rays generated from a thick solid sample are decreased by the attenuation of energy of the incident protons and the absorption of the X-rays by the sample matrix, comparing with results of PIXE measurements for a thin-film material. In this model, the decrease of total X-ray intensities from the whole sample volume irradiated by the proton beam are calculated by considering the beam sizes and the beam penetration, the major element composition, a density of the matrix, their proton-stopping powers, the X-ray production cross sections, and the X-ray absorption coefficients. Finally, element concentrations are calculated based on X-ray intensities corrected for the decrease and the detector sensitivity determined for each element. The detector sensitivity in this study were determined by measurements of thin-film multielement reference samples and a multi-element reference glass material NIST SRM 1412. The thin-film sample was prepared by dropping several standard solutions for ICP analysis onto a Mylar film and drying the film in a desiccator. By using the calculation model, almost trace elements in solid sample at levels of a few to several thousands ppm can be determined with the total analytical error of 10–15 % [8].

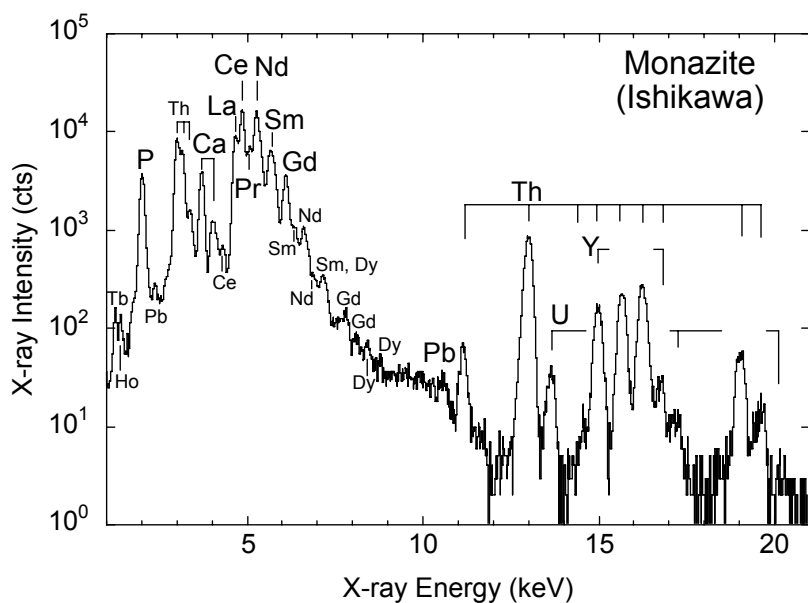


Fig.1. PIXE spectrum of monazite from Ishikawa, Japan

X-rays excited by the incident beam were collected by the Si(Li) X-ray-energy detector (Gresham Co.) with a nominal resolution of 154 eV at 5.9 keV, and the spectra were recorded by a multi-channel analyzer. A 55- μm -thick Mylar film was used to attenuate the intense X-rays from the light elements and to prevent the entry into the detector of protons scattered from samples. The total charge was determined by integrating the target currents, and all samples were analyzed to

the integrated charges of 0.15 to 0.37 μC . Analytical points were chosen based on optical viewing using a CCD camera mounted on the microscope [9].

Results

Observed spectrum of the monazite consisted mainly of the K-X ray peaks from P, Ca, and Y, the L-X ray peaks from La, Ce, Nd, Pr, Sm, Gd, Dy, Pb, Th and U, and the M-X ray peaks from Tb, Ho, Pb and Th (Fig. 1). Determined concentrations of the monazite agreed well with the values determined by EPMA. In addition, a chondrite-normalized REE pattern of the PIXE result is very smooth and agreed well with that determined by Laser Ablation-ICP-MS [10]. Hence, the present PIXE values are thought to be reasonable and accurate. This result indicates a suitable subtraction of overlapped L X-ray peaks from interest REE peaks. The future works are determinations of REE contents in the other rare-element minerals using this method and evaluations of granitic pegmatites as a potential REE resource in this area.

References

- [1] K. Suzuki and M. Adachi, *Geochem. J.*, 25 (1991), 357.
- [2] A. K. Mohanty et al., *Nucl. Instr. and Meth.*, B211 (2003), 145.
- [3] J. H. Scofield, *Phys. Rev.*, A9 (1974) 1041.
- [4] J. L. Campbell et al, *Nucl. Instr. and Meth.*, B43 (1989), 197.
- [5] D. D. Cohen and M. Harrigan *At. Data Nucl. Data*, 34 (1986), 393.
- [6] M. A. Reis and A. P. Jesus, *At. Data Nucl. Data*, 63 (1996), 1.
- [7] J. L. Campbell, In: *Particle-Induced X-ray Emission Spectrometry (PIXE)*, John Wiley, (1995) 19.
- [8] M. Kurosawa et al., *Geostand. Geoanal. Res.*, 30 (2006), 17.
- [9] M. Kurosawa et al., *Nucl. Instr. and Meth. B*142 (1998), 599.
- [10] T. Nakajima and M. Kurosawa, *Can. Mineral.*, 44 (2006), 31.

5.3 Ion induced nanoparticle formation in N₂/H₂O/SO₂

M. Fujieda, S. Kanda, M. Matsuoka, M. Imanaka¹, K. Sasa, S. Tomita, H. Kudo

The mechanism of ion induced nanoparticle formation attracts a lot of attention because of the possible correlation between the Earth's total low-altitude cloud cover and galactic cosmic ray flux [1]. SO₂ gas is believed to have an important role in the mechanism. To study the effect of SO₂, we irradiated 20 MeV protons in gas mixture of N₂/H₂O/SO₂, and measured the size distribution of produced nanoparticles. The experiments were performed with a tandem accelerator at University of Tsukuba. The size distributions were obtained by measuring the electrical mobility of charged nanoparticle with a differential mobility analyzer.

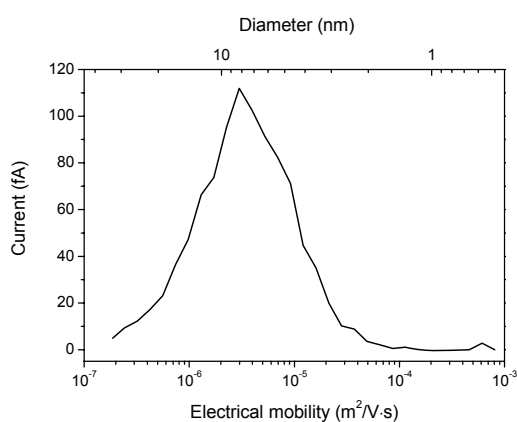


Fig.1. Electrical mobility spectrum of positively charged nanoparticle nucleated by irradiation of 20 MeV proton in N₂/H₂O/SO₂

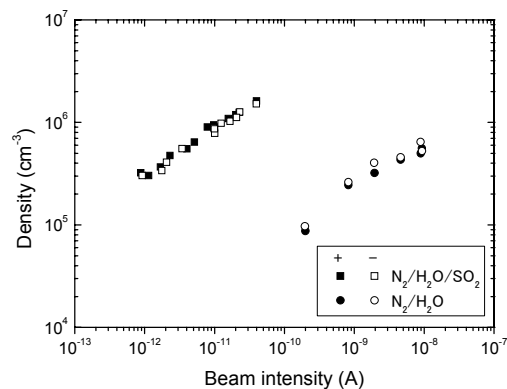


Fig.2. Density of nanoparticle in N₂/H₂O and N₂/H₂O/SO₂,

The electrical mobility spectrum of positively charged particle is shown in Fig. 1. The distribution has a peak at electrical mobility of $3 \times 10^{-6} \text{ m}^2/(\text{V} \cdot \text{s})$, which corresponds to a diameter of about 8 nm. A similar spectrum was obtained for negatively charged particles. The density of produced nanoparticles is given by the area under the spectrum, which is shown in Fig.2 as a function of the intensity of the proton beam. It is clearly seen that the density is higher than for N₂/H₂O by a factor of more than 10. The enhancement is due to sulfuric acid, that was produced through oxidation reaction of SO₂. The oxidation reaction takes place with help of OH radicals which are produced by proton irradiation.

References

[1] H. Svensmark and E. Friis-Christensen, *J. Atmos. Solar Terr. Phys.* 59,1225 (1997)

¹ RIKEN, Wako, Saitama, 351-0198, Japan

6. LIST OF PUBLICATIONS

The publications listed here are those released in the fiscal year 2007 by all the workers listed on p.57.

6.1 Journals

NUCLEAR PHYSICS

1. Kosuke Morita, Kouji Morimoto, Daiya Kaji, Takahiro Akiyama, Sin-ichi Goto, Hiromitsu Haba, Eiji Ideguchi, Kenji Katori, Hiroyuki Koura, Hisaaki Kudo, Tetsuya Ohnishi, Akira Ozawa, Toshimi Suda, Keisuke Sueki, Fuyuki Tokanai, Takayuki Yamaguchi, Akira Yoneda, and Atsushi Yoshida, Experiment on Synthesis of an Isotope $^{277}112$ by $^{208}\text{Pb}+^{70}\text{Zn}$ Reaction, J. Phys. Soc. Jpn., Vol. 76, No. 4, p.043201(2007).
2. D.Q.Fang, W.Guo, C.W.Ma, K.Wang, T.Z.Yan, Y.G.Ma, X.Z.Cai, W.Q.Shen, Z.Z.Ren, Z.Y.Sun, J.G.Chen, W.D.Tian, C.Zhong, M.Hosoi, T.Izumikawa, R.Kanungo, S.Nakajima, T.Ohnishi, T.Ohtsubo, A.Ozawa, T.Suda, K.Sugawara, T.Suzuki, A.Takisawa, K.Tanaka, T.Yamaguchi, and I.Tanihata, Examining the exotic structure of the proton-rich nucleus ^{23}Al , Phys. Rev. C 76, 031601(R) (2007).
3. M. Iijima, Y. Aoki, A. Ozawa, N. Okumura, CDCC analysis of $^{118}\text{Sn}(d, p)$ reaction below Coulomb barrier, Nucl. Phys. A 793 (2007) 79-95.
4. M. Notani, H. Sakurai, N. Aoi, H. Iwasaki, N. Fukuda, Z. Liu, K. Yoneda, H. Ogawa, T. Teranishi, T. Nakamura, H. Okuno, A. Yoshida, Y. X. Watanabe, S. Momota, N. Inabe, T. Kubo, S. Ito, A. Ozawa, T. Suzuki, I. Tanihata, and M. Ishihara, Projectile fragmentation reactions and production of nuclei near the neutron drip line, Phys. Rev. C 76, 044605 (2007).
5. C.B. Moon, C.S. Lee, T. Komatsubara, Y. Sasaki, K. Furuno, Structure of the negative parity bands in Xe-125, Phys. Rev. C 76 067301 (2007).
6. S.Y. Wang, Y.Z. Liu, Y.J. Ma, T. Komatsubara, Y.H. Zhang, Observation of negative-parity high spin states of Cs-126, Phys. Rev. C 75 037302 (2007)

MATERIALS AND CLUSTER SCIENCE

7. P. Hvelplund, B. Liu, S. Brøndsted Nielsen, and S. Tomita, Formation of higher-order fullerene dianions in collisions with Na atoms Eur. Phys. J. D 43, (2007) 133-136
8. Henning Zettergren, Henning T. Schmidt, Peter Reinhed, Henrik Cederquist, Jens Jensen, Preben Hvelplund, Shigeo Tomita, Bruno Manil, Jimmy Rangama, Bernd A. Huber, Stabilities of multiply charged dimers and clusters of fullerenes, J. Chem. Phys. 126, (2007) 224303(1-8)

9. H. Zettergren, H. T. Schmidt, P. Reinhed, H. Cederquist, J. Jensen, P. Hvelplund, S. Tomita, B. Manil, J. Rangama, B. A. Huber, Even-odd effects in the ionization cross sections of $[C_{60}]_2$ and $[C_{60}C_{70}]$ dimers, *Phys. Rev. A* 75, (2007) 051201(R) (1-4)
10. S. Tomita, Y. Sato, M. Ohkubo, M. Ukibe, S. Hayakawa, Pulse height reduction effects of superconducting tunnel junction particle detectors for low-energy light molecular ions, *Appl. Phys. Lett.* 91, (2007) 053507 (1-3)
11. Eiji Kita, K. Shibata, H. Yanagihara, Y. Sasaki, M. Kishimoto, Magnetic Properties of Core-Shell Type $Fe_{16}N_2$ Nanoparticles, *J. Magn. Magn. Mater.*, 310 (2007) 2411-2413.
12. Manabu Hasegawa, H. Yanagihara, Yuta Toyoda, Eiji Kita, L. Ranno, Electrical and magnetic properties of g- Fe_2O_3 epitaxial films, *J. Magn. Magn. Mater.*, 310 (2007) 2283-2285.
13. T. Katayama, D. Sekiba, K. Mukai, Y. Yamashita, F. Komori, J. Yoshinobu, Adsorption States and Dissociation Processes of Oxygen Molecules on Cu(100) at Low temperature, *The Journal of Physical Chemistry C*, 111, 15059-15063, 2007
14. D. Sekiba, F. Komori, P. Cortona, Investigation of the surface bands along the X-M line of the Cu(100) surface, *Physical Review B*, 75, 165410-1-7, 2007
15. D. Sekiba, H. Yonemura, T. Nebiki, S. Ogura, M. Wilde, M. Matsumoto, T. Okano, J. Kasagi, T. Narusawa, S. Kuribayashi, Y. Iwamura, T. Ito, H. Matsuzaki, K. Fukutani, Development and Application of Micro-beam Nuclear Reaction Analysis for Observation of Hydrogen Distribution, *Journal of Vacuum Society of Japan*, 50, 574-578, 2007

ACCELERATOR MASS SPECTROMETRY

16. Ming He, Shan Jiang, Yasuo Nagashima, Yaoyun Yanga, Tsutomu Takahashi, Kexin Liuc, Kimikazu Sasa, Kejun Dong, Shaoyong Wu, Takeshi Matsuhira, Yuuki Tosaki, Xiaotang Ren, Riki Seki and Keisuke Sueki, AMS measurement of ^{26}Al cross section for the reaction $^{14}N(^{16}O, \alpha)^{26}Al$, *Nucl. Inst. Meth. B*, 259, 629-631, (2007).
17. Yasuo Nagashima, Riki Seki, Kimikazu Sasa, Takeshi Matsuhira, Tsutomu Takahashi, Yuki Tosaki, Koutaro Bessho, Hiroshi Matsumura, Taichi Miura, ^{129}I AMS by a $^{97}Mo^{16}O_2$ molecular pilot beam method, *Nucl. Inst. Meth. B*, 259, 241-245, (2007).
18. R. Seki, T. Matsuhira, Y. Nagashima, T. Takahashi, K. Sasa, K. Sueki, Y. Tosaki, K. Bessho, H. Matsumura, T. Miura, Isotopic ratios of $^{36}Cl/Cl$ in Japanese surface soil, *Nucl. Inst. and Meth. B*, 259, 486-490, (2007).
19. K. Bessho, H. Matsumura, T. Miura, Q. Wang, K. Masumoto, H. Hagura, Y. Nagashima, R. Seki, T. Takahashi, K. Sasa, K. Sueki, T. Matsuhira, Y. Tosaki, Estimation of thermal neutron

- fluences in the concrete of proton accelerator facilities from ^{36}Cl production, Nucl. Inst. Meth. B, 259, 702-707, (2007).
20. Yuki Tosaki, Norio Tase, Gudrun Massmann, Yasuo Nagashima, Riki Seki, Tsutomu Takahashi, Kimikazu Sasa, Keisuke Sueki, Takeshi Matsuihiro, Taichi Miura, Kotaro Bessho, Hiroshi Matsumura, Ming He, Application of ^{36}Cl as a dating tool for modern groundwater, Nucl. Inst. Meth. B, 259, 479-485, (2007).
 21. Kimikazu Sasa, Yasuo Nagashima, Tsutomu Takahashi, Riki Seki, Yuki Tosaki, Keisuke Sueki, Kotaro Bessho, Hiroshi Matsumura, Taichi Miura, Ming He, ^{26}Al and ^{36}Cl AMS system at the University of Tsukuba: A progress report, Nucl. Inst. Meth. B, 259, 41-46, (2007).
 22. B. Zhou, Y. Nagashima, S. Jiang, W. Wu, Y. Guan, S. Wu, M. He, J. Yuan, X. Ruan, R. Seki, K. Sasa, T. Takahashi, Y. Tosaki, Y. Matsushi, M. Tamari, and K. Sueki, An improved method for ^{129}I -AMS measurement, Nuclear Electronics & Detection Technology (China), Vol. 27(4), 740-744, (2007).
 23. Yuki Tosaki, Norio Tase, Masaya Yasuhara, Yasuo Nagashima, Kimikazu Sasa and Tsutomu Takahashi, An Estimate of Local Bomb-Produced ^{36}Cl Fallout Using the Depth Profile of Groundwater in the Tsukuba Upland, Central Japan, Hydrological Research Letters, Vol. 2, pp.9-13, (2008).
 24. Yasuo Nagashima, Riki Seki, Kimikazu Sasa, Tsutomu Takahashi, An Accelerator Mass Spectrometry by the Large Tandem Electrostatic Accelerator, Journal of the Vacuum Society of Japan. Vol.50, No.7, 475-479, (2007).

INTERDISCIPLINARY RESEARCH

25. Y. Oguri, J. Hasegawa, M. Ogawa, J. Kaneko and K. Sasa, A Phantom Test of Proton-Induced Dual-Energy X-Ray Angiography Using Iodinated Contrast Media, International J. of PIXE Vol.17, Issue 1/2, 11-21, (2007).

6.2 International conferences

1. Kimikazu Sasa (Invited talk), Cosmogenic Cl-36 measurements with the Tsukuba AMS system and the application as a dating tool for Antarctic deep ice core. Kochi University-KIGAM International Symposium, Kochi University, 21-22 February, 2008.
2. Kimikazu Sasa, Satoshi Ishii, Masanori Kurosawa, Micro PIXE system for trace element analysis of single fluid inclusions in mineral samples, 9th European Conference on Accelerators in Applied Research and Technology, September 3-7, 2007, Florence, ITALY.
3. K. Sasa, Measurement of ^{36}Cl with the Tsukuba AMS system: its applications in earth and environmental sciences, The 2nd East Asia Accelerator Mass Spectroscopy Conference, the Seoul National University and the KIGAM (Korea Institute of Geology and Mineral Resources), 22-23 October, 2007.
4. Seung Jun Yu, Yoshimichi Ohki, Makoto Fujimaki, Kouichi Awazu, Junji Tominaga, Kimikazu Sasa, Tetsuro Komatsubara, Reduction of Polarization Dependent Loss of a Planar Optical Waveguide using Ion Implantation, MRS(Materials Research Society) 2008 Spring meeting, March 24-28, Moscone West and San Francisco Marriott.
5. S. Tomita, M. Imanaka, S. Kanda, M. Fujieda, K. Sasa and H. Kudo, Formation of nanodroplets from $\text{N}_2/\text{H}_2\text{O}$ by irradiation of 20 MeV protons, ISIAC2007, 20th International Symposium on Ion - Atom Collisions, XX ISIAC, August 1-4, 2007, Agios Nikolaos, Crete, GREECE.
6. T. Komatsubara, K. Sasa, M. Kurosawa, S. Ishii, Y. Yamato, K. Ebisu, T. Kawamata, Hydrogen analysis by proton-proton elastic recoil coincidence spectrometry, International Nuclear Physics Conference, Tokyo, Japan, June 3-8, 2007
7. A. Ozawa, Mass measurements by isochronous storage ring in RI beam factory, International Nuclear Physics Conference, Tokyo, Japan, June 3-8, 2007
8. K. Hara, Photonuclear reaction cross sections for ^{37}Cl and ^{152}Sm , International Nuclear Physics Conference, Tokyo, Japan, June 3-8, 2007
9. Y. Yasuda, Measurement of deep hole states in ^{39}K by (p,2p) reaction at $E_p=392$ MeV, International Nuclear Physics Conference, Tokyo, Japan, June 3-8, 2007
10. M. Iijima, $^{118}\text{Sn}(\text{d},\text{p})$ reaction below Coulomb barrier International Nuclear Physics Conference, Tokyo, Japan, June 3-8, 2007
11. D. Sekiba, H. Yonemura, T. Nebiki, S. Ogura, M. Wilde, M. Matsumoto, T. Okano, J. Kasagi, T. Narusawa, S. Kuribayashi, Y. Iwamura, T. Ito, H. Matsuzaki, K. Fukutani, Micro-beam NRA for 3D mapping of hydrogen distribution in solids (oral), 18th International Conference on Ion Beam Analysis (Hyderabad, India, 23 September 2007)

7. THESES

M. Sc. Theses

Suguru Kanda	Mechanism of droplet formation induced by proton irradiation
Makoto Minagawa	Synthesis and magnetic properties of iron nitride particles prepared from sub-micron sized Fe ₃ O ₄ particles
Kazuya Ebisu	Improvement of hydrogen analysis by using high energy proton micro beam
Tetsuaki Moriguchi	Studies of Hybrid Photo Detector to measure time-of-flight of RI beams
Tomohito Kawamata	Effect of multiple scattering in ERCS hydrogen analysis
Yuhei Hashizume	Measurements of momentum distributions of fragments from C isotopes located near the neutron drip line
Takeshi Hoya	Measurements of reaction cross sections of ³ He and ³ H at intermediate energies

8. SEMINARS

<u>Date</u>		<u>Title and Speaker</u>
2007		
May	9	Unstable nucleus ^{151}Sm and s-process <i>Kaoru Hara (Univ. of Tsukuba)</i>
Oct	12	Penning trap mass spectrometry of short-lived isotopes <i>Peter H. Schury (RIKEN)</i>
Oct	16	Tevatron optics measurements using an AC dipole <i>Ryoichi Miyamoto (Texas Austin)</i>
Oct	26	The measurement of ^{41}Ca with AMS and its application at CIAE <i>Jiang Shan (CIAE)</i>
2008		
Jan	9	Improvement of hydrogen analysis by using high energy proton micro beam <i>Kazuya Ebisu (Univ. of Tsukuba)</i>
Jan	9	Development of high voltage control system and performance evaluation of transition radiation detector for LHC-ALICE experiment <i>Kengo Watanabe (Univ. of Tsukuba)</i>
Jan	16	Studies of Hybrid Photo Detector to measure time-of-flight of RI beams <i>Tetsuaki Moriguchi (Univ. of Tsukuba)</i>
Jan	16	Evaluation of Multi-Gap Resistive Plate Chamber for the use of High Energy Heavy Ion Collision Experiments <i>Takanori Sato (Univ. of Tsukuba)</i>
Jan	23	Effect of multiple scattering in ERCS hydrogen analysis <i>Tomohito Kawamata (Univ. of Tsukuba)</i>
Jan	30	Measurements of momentum distributions of fragments from C isotopes located near the neutron drip line <i>Yuhei Hashizume (Univ. of Tsukuba)</i>
Jan	30	Measurements of reaction cross sections of ^3He and ^3H at intermediate energies <i>Takeshi Hoya (Univ. of Tsukuba)</i>
Feb	13	Systematic study of azimuthal anisotropy for PID charged Hadrons in relativistic heavy ion collisions <i>Maya Shimomura (Univ. of Tsukuba)</i>
Mar	12	Recent development of AMS study in China Institute of Atomic Energy <i>He Ming (CIAE)</i>

9. SYMPOSIA

Workshop on "r-process nucleosynthesis and quantum beam"

13,14 March, 2008

University Hall, Conference Room

hosted by National Astronomical Observatory of Japan

1. Opening : A. Ozawa (Univ. of Tsukuba)
2. What would be the best method for producing nuclei along the r-process path? : I. Tanihata (RCNP)
3. Nuclear physics studies for r-process nucleosynthesis at RIKEN RI Beam Factory : T. Motobayashi (RIKEN)
4. Present status of Rare-RI Ring : Y. Yamaguchi (RIKEN)
5. Recent developments on low-energy radioisotope beam production at CNS-CRIB : H. Yamaguchi (CNS)
6. Nucleosynthesis study with real photon beams : H. Utsunomiya (Konan Univ.)
7. Investigation of origin of p-process isotopes using reactor neutrons, laser Compton scattering gamma-rays and tandem ions : T. Hayakawa (JAEA)
8. Study of nuclear synthesis of ^{26}Al by gamma ray spectroscopy : T. Komatsubara (Univ. of Tsukuba)
9. Systematic calculations of electric dipole response with mean-field approach : T. Itakura (Univ. of Tsukuba)
10. Fission barrier for heavy neutron-rich nuclei using with Skyrme-Hartree-Fock : F. Minato (Tohoku Univ.)
11. $^{118}\text{Sn}(d,p)$ reaction below Coulomb barrier : M. Iijima (Univ. of Tsukuba)
12. Astrophysical nuclear reactions and cluster models : K. Kato (Hokkaido Univ.)
13. Big bang nucleosynthesis catalyzed by a SUSY-particle stau : M. Kamimura (Kyushu Univ./RIKEN)
14. Nuclear astrophysics at TRIAC facility : H. Miyatake (KEK)
15. Present status of $^{12}\text{C}+^4\text{He}\rightarrow^{16}\text{O}+\gamma$ experiment at KUTL : K. Sagara (Kyushu Univ.)
16. Measurement of the E1 and E2 cross sections of the $^{12}\text{C}(\alpha,\gamma)^{16}\text{O}$ reaction using pulsed alpha beams : H. Makii (JAEA)
17. Explosive nucleosynthesis in GRB : T. Kajino (NAO)
18. Supernova explosion and nucleosynthesis : G.J. Mathews (Univ. Notre Dame)
19. Supernova neutrino nucleosynthesis : T. Yoshida (NAO)
20. The r-process in neutrino-driven winds : S. Wanajo (Tokyo Univ.)
21. Neutron capture elements and astronomical observation : W. Aoki (NAO)
22. Closing : T. Kajino (NAO)

Annual meeting of UTTAC users
Seeds for new application of high quality ion beams
- Tendency and Results of the UTTAC Research Works 2007 -

17 March, 2008

Laboratory of Advanced Research B 0110

1. Opening : *H. Kudo (Univ. of Tsukuba)*
2. Origin of life and synthesis of organic matter with particle irradiation on quasi-cosmic dust (Invited) : *N. Kobayashi (Yokohama National Univ.)*
3. Li diffusion studies in lithium ionic conductors using the short-lived radiotracer of ^8Li (Invited) : *S.C. Jeong (KEK)*
4. Present status of production of ^8Li at UTTAC : *K. Hara (Univ. of Tsukuba)*
5. Research for excited states in ^{26}Si : *T. Komatsubara (Univ. of Tsukuba)*
6. Supernova neutrino-process nuclide ^{138}La : *T. Hayakawa (JAEA)*
7. Average charge and its structure dependence of carbon cluster ion under irradiation of thin foils (Invited) : *A. Chiba (JAEA)*
8. Energy loss of fast cluster ions in thin carbon foils : *S. Tomita (Univ. of Tsukuba)*
9. Waveguide mode biosensors fabricated with swift heavy ions : *K. Awazu (AIST)*
10. Effects of ionized radiation from the outer space for the stratosphere : What we may explore through laboratory experiments (Invited) : *Y. Nakai (RIKEN)*
11. Water droplet formation under irradiation of proton beam : *M. Imanaka (RIKEN)*
12. Accelerator Mass Spectrometry and its application for earth environmental sciences (Invited) : *H. Matsuzaki (Tokyo Univ.)*
13. Cosmogenic ^{36}Cl variations over the past 720 kyr in the Dome Fuji ice core, Antarctica : *K. Sasa (Univ. of Tsukuba)*
14. In-situ-produced cosmogenic ^{36}Cl in calcite : *Y. Matsushi (Tokyo Univ.)*
15. Analysis of Chlorine-36 in meteorite : *Y. Oura (Tokyo Metropolitan Univ.)*
16. In situ observation of defect production during ion irradiation by positron annihilation spectroscopy (Invited) : *H. Tsuchida (Kyoto Univ.)*
17. Point defects in Er-doped GaN probed by a monoenergetic positron beam (Invited) : *A. Uedono (Univ. of Tsukuba)*
18. Micro-analysis of hydrogen near metal surface by using ERCS and NRA : *D. Sekiba (Univ. of Tsukuba)*
19. PIXE analysis of liquid inclusion : *M. Kurosawa (Univ. of Tsukuba)*

10. LIST OF PERSONNEL

Tandem Accelerator Complex

H. Kudo	Director, Professor
T. Komatsubara	Assistant Professor
K. Sasa	Assistant Professor
D. Sekiba	Assistant Professor
S. Ishii	Mechanical Engineer
H. Kimura	Computer Engineer
H. Oshima	Electric Engineer
Y. Tajima	Mechanical Engineer
T. Takahashi	Electric Engineer
Y. Yamato	Electric Engineer
Y. Tagishi	Research Coordinator
Y. Nagashima	Research Coordinator
K. Hara	Research Fellow
S. Mihara	Research Fellow
T. Oki	Research Fellow
Y.J. Guan	Research Fellow
M. Matsumura	Technical Assistant
M. Moro	Administrative Staff

Steering Committee

H. Kudo	Y. Miake	T. Sakae	K. Matsukura	K. Murakami
A. Ozawa	T. Komatsubara	K. Sasa	D. Sekiba	

Research Members ¹

Inst. of Physics

I. Arai	T. Komatsubara	M. Onoda	A. Ozawa	K. Sasa
Y. Yasuda				

Inst. of Applied Physics

S. Aoki	K. Akimoto	E. Kita	H. Kudo	T. Makimura
T. Suemasu	S. Tomita	A. Uedono	H. Yanagihara	

Inst. of Materials Science

T. Kondo	J. Nakamura	H. Mizubayashi	H. Tanimoto
----------	-------------	----------------	-------------

Inst. of Engineering Mechanics and Systems

K. Matsuuchi

¹The "research members" include the authors and coauthors within 5 years back from this fiscal year, as well as the members of research projects running at UTTAC.

Inst. of Geoscience

M. Kurosawa N. Tase

Inst. of Chemistry

K. Sueki

Graduate students

Doctoral Programs of Pure and Applied Science

H. Arai	S. Igarashi	M. Iijima	T. Ikeda	Y. Ikeda
M. Konno	H. Masui	K. Miki	T. Miyazawa	M. Nakazumi
J.P. Oh	M. Oka	J.W. Seo	M. Shimomura	K. Takao
H. Tanaka	K. Yamaguchi			

Master's Programs of Pure and Applied Science

K. Ebisu	M. Fujieda	Y. Funagi	I. Goto	J. Hagiwara
Y. Hashizume	T. Hoya	K. Ito	S. Kanda	S. Kouso
K. Maeda	T. Maekoya	M. Minakawa	Y. Mizuguchi	T. Moriguchi
M. Murakami	K. Muto	A. Onishi	W. Onoda	D. Sakata
M. Sano	Y. Sato	N. Seya	A. Shimao	N. Shiobara
A. Sugawara	A. Suzuki	H. Suzuki	M. Tamari	N. Umada
K. Watahiki	K. Watanabe	K. Yamada	D. Yoshioka	

Doctoral Programs of Life and Environmental Sciences

Y. Tosaki

Master's Program in Education

T. Kawamata

Undergraduates

T. Adachi	E. Hamada	M. Hashimoto	M. Honda	M. Horikoshi
T. Ikuyama	Y. Ito	Ho Jo	M. Kajitani	Y. Kaku
M. Matsuoka	K. Muto	K. Ogawa	T. Okuyama	T. Shiba
Y. Seto	A. Takashima	N. Udeda	T. Watanabe	T. Waki
H. Yokoyama				

Scientific Guests and Fellows

K. Awazu	AIST
M. Fujimaki	AIST
S.J. Yu	Waseda Univ.
K. Sugimoto	Waseda Univ.
H. Aiba	Waseda Univ.
Y. Koganezawa	Waseda Univ.
K. Nomura	Waseda Univ.
A. Maeda	Waseda Univ.
S. Fujii	Waseda Univ.
Y. Matsumoto	Tokyo Univ.
H. Muramatsu	KEK
K. Bessho	KEK
K. Masumoto	KEK
N. Kinoshita	KEK
I. Sugai	KEK
H. Kawakami	KEK
M. Oyaizu	KEK
Y. Takeda	KEK
T. Hayakawa	JAEA
T. Shizuma	JAEA
H. Matsuki	JAXA
T. Komiyama	JAXA
Y. Sasaki	JAXA
Y. Terakado	Meisei Denki
M. Nakazawa	Meisei Denki
M. Kusakabe	Meisei Denki
S. Mizumoto	Meisei Denki
M. Tomitaka	Meisei Denki
S. Kubono	CNS
H. Yamaguchi	CNS
Y. Wakabayashi	CNS
S. Hayakawa	CNS
Y. Kurihara	CNS
Y. Ohura	Tokyo Metropolitan Univ.
H. Hashizume	Tokyo Metropolitan Univ.
Y. Matsushi	Tokyo Univ.
J. Asai	RIKEN
R. Ichimiya	RIKEN
K. Kurita	Rikkyo Univ.
M. Kawashima	Rikkyo Univ.
K. Sakashita	Tokyo Institute of Technology
N. Okumura	Nagano College of Technology
N. Imai	KEK
H. Ishiyama	KEK
Y. Watanabe	KEK
Y. Hirayama	KEK
H. Sato	Ibaraki Univ.